Title
Radar attenuation and temperature within the Greenland Ice Sheet

Journal
Journal of Geophysical Research Earth Surface, 120(6)

ISSN
2169-9003

Authors
MacGregor, Joseph A
Li, Jilu
Paden, John D
et al.

Publication Date
2015-06-01

DOI
10.1002/2014jf003418

Peer reviewed

AGU PUBLICATIONS

JGR

Journal of Geophysical Research: Earth Surface

RESEARCH ARTICLE

10.1002/2014JF003418

Key Points:

- The pattern of radar attenuation within the Greenland Ice Sheet was mapped
- Patterns of radar attenuation are related to englacial temperature
- Radar-inferred temperatures are lower than modeled in southern Greenland

Correspondence to:
J. A. MacGregor,
joemac@ig.utexas.edu

Citation:
MacGregor, J. A., et al. (2015), Radar attenuation and temperature within the Greenland Ice Sheet, *J. Geophys. Res. Earth Surf.*, *120*, doi:10.1002/2014JF003418.

Received 15 DEC 2014
Accepted 27 APR 2015
Accepted article online 30 APR 2015

Radar attenuation and temperature within the Greenland Ice Sheet

Joseph A. MacGregor[1], Jilu Li[2], John D. Paden[2], Ginny A. Catania[1,3], Gary D. Clow[4,5], Mark A. Fahnestock[6], S. Prasad Gogineni[2], Robert E. Grimm[7], Mathieu Morlighem[8], Soumyaroop Nandi[2], Hélène Seroussi[9], and David E. Stillman[7]

[1]Institute for Geophysics, University of Texas at Austin, Austin, Texas, USA, [2]Center for Remote Sensing of Ice Sheets, University of Kansas, Lawrence, Kansas, USA, [3]Department of Geological Sciences, University of Texas at Austin, Austin, Texas, USA, [4]U.S. Geological Survey, Lakewood, Colorado, USA, [5]Institute for Arctic and Alpine Research, University of Colorado Boulder, Boulder, Colorado, USA, [6]Geophysical Institute, University of Alaska Fairbanks, Fairbanks, Alaska, USA, [7]Department of Space Studies, Southwest Research Institute, Boulder, Colorado, USA, [8]Department of Earth System Science, University of California, Irvine, California, USA, [9]Jet Propulsion Laboratory, California Institute of Technology, Pasadena, California, USA

Abstract The flow of ice is temperature-dependent, but direct measurements of englacial temperature are sparse. The dielectric attenuation of radio waves through ice is also temperature-dependent, and radar sounding of ice sheets is sensitive to this attenuation. Here we estimate depth-averaged radar-attenuation rates within the Greenland Ice Sheet from airborne radar-sounding data and its associated radiostratigraphy. Using existing empirical relationships between temperature, chemistry, and radar attenuation, we then infer the depth-averaged englacial temperature. The dated radiostratigraphy permits a correction for the confounding effect of spatially varying ice chemistry. Where radar transects intersect boreholes, radar-inferred temperature is consistently higher than that measured directly. We attribute this discrepancy to the poorly recognized frequency dependence of the radar-attenuation rate and correct for this effect empirically, resulting in a robust relationship between radar-inferred and borehole-measured depth-averaged temperature. Radar-inferred englacial temperature is often lower than modern surface temperature and that of a steady state ice-sheet model, particularly in southern Greenland. This pattern suggests that past changes in surface boundary conditions (temperature and accumulation rate) affect the ice sheet's present temperature structure over a much larger area than previously recognized. This radar-inferred temperature structure provides a new constraint for thermomechanical models of the Greenland Ice Sheet.

1. Introduction

The creep of ice and the potential for basal sliding beneath ice sheets both depend critically on englacial temperature [*Cuffey and Paterson*, 2010]. Knowledge of temperature within ice sheets is therefore valuable for accurate modeling of ice-sheet flow. Mapping the thermal state of the bed beneath the Greenland and Antarctic ice sheets is also important, because this state is poorly known but essential for estimating the contribution of ice sheets to future sea-level rise [e.g., *Alley et al.*, 2005; *Nowicki et al.*, 2013]. Analysis of internal and basal reflections recorded by radar sounding suggests spatially variable basal melt and freeze-on and hence significant heterogeneity in the temperature structure of ice sheets [e.g., *Fahnestock et al.*, 2001; *Dahl-Jensen et al.*, 2003; *Carter et al.*, 2009; *Bell et al.*, 2014; *Fujita et al.*, 2012; *Oswald and Gogineni*, 2012; *Schroeder et al.*, 2014]. Thermomechanical modeling also predicts significant spatial variability in ice-sheet temperature [e.g., *Greve*, 2005; *Pattyn*, 2010; *Rogozhina et al.*, 2011, 2012; *Aschwanden et al.*, 2012; *Seroussi et al.*, 2013].

Direct measurement of englacial temperature generally requires borehole drilling, which is logistically complex and may require a year or longer for the borehole temperature to equilibrate after drilling. Despite these challenges, borehole-measured temperatures have produced evidence of spatiotemporal variability in ice-sheet temperature that informs our understanding of ice-sheet flow and history [e.g., *Funk et al.*, 1994; *Cuffey and Clow*, 1997; *Dahl-Jensen et al.*, 1998; *Engelhardt*, 2004]. Remote geophysical observations are an indirect alternative to measuring englacial temperature in sparse boreholes. *Peters et al.* [2012] showed that temperature within the Greenland Ice Sheet (GrIS) can be inferred from seismic reflections using knowledge of the temperature dependence of the englacial attenuation of seismic waves. The dielectric attenuation of radio waves through ice is also temperature dependent, and this temperature dependence is arguably better constrained than for englacial seismic attenuation [*MacGregor et al.,* 2007; *Stillman et al.,* 2013a]. Hence, inferences of radar attenuation from existing radar data, which are extensive across both ice sheets, could improve our knowledge of their temperature structure significantly.

Models and observations of radar attenuation through polar ice sheets are increasing in number and methodology [*Matsuoka et al.,* 2010a], including analysis of airborne radar-sounding data [*Matsuoka et al.,* 2010b]. Although the spatial variation of radar attenuation is somewhat affected by ice chemistry, modeling predicts that its spatial variation is controlled primarily by temperature [*Corr et al.,* 1993; *Matsuoka et al.,* 2010b, 2012; *Matsuoka*, 2011; *MacGregor et al.,* 2012]. Most existing in situ estimates are qualitatively consistent with expected variability in englacial temperature. For example, estimates of inland East Antarctic radar-attenuation rates are typically less than half (in units of dB km^{-1}) of those in West Antarctica, where ice is typically thinner and the surface temperature is warmer [*MacGregor et al.,* 2007, 2011; *Jacobel et al.,* 2009, 2010; *Zirizzotti et al.,* 2014]. Fewer radar-attenuation estimates exist for the GrIS [*Paden et al.,* 2005; *Christianson et al.,* 2014].

Several studies have considered the possibility of inferring englacial temperature from ice-penetrating radar data [*Robin et al.,* 1969; *Bogorodsky et al.,* 1985; *Hughes*, 2008], but none have yet done so rigorously nor applied a specific method to the large volume of data now collected over either polar ice sheet. *Matsuoka et al.* [2010b] estimated depth-averaged radar-attenuation rates in West Antarctica from the echo intensity of internal reflections, but they could not directly attribute spatial variability in these estimates to changing englacial temperature. Here we estimate the spatial pattern of radar attenuation within the GrIS using an ice-sheet-wide airborne ice-penetrating radar data set. Using empirical models, we relate this radar-attenuation pattern to borehole-measured temperature to then infer the temperature structure of this ice sheet.

2. Data

2.1. Ice-Penetrating Radar Data and Radiostratigraphy

We use the same ice-penetrating radar data set whose internal reflections (radiostratigraphy) were mapped by *MacGregor et al.* [2015]. These radar data, their traced radiostratigraphy, and the dating of that radiostratigraphy are described in detail by that study. These data were collected across the GrIS using an evolving set of ice-penetrating radars developed by The University of Kansas (KU). These radars were deployed during several multiyear campaigns, of which the most recent, extensive, and critical to this study is NASA's Operation IceBridge. Internal reflections were semiautomatically traced by following the peak echo intensity P_r of an identified reflection, which is the quantity that we analyze in this study.

The radar data traced by *MacGregor et al.* [2015] were focused using synthetic aperture radar (SAR) techniques after combining the received signal from multiple channels in response to multiple transmitted chirps. The method of estimating radar attenuation described below requires only that the traced reflections within any given trace be radiometrically calibrated with respect to each other, i.e., in a relative sense. This requirement limits the portion of the GrIS radiostratigraphy that can be used to estimate radar attenuation, because not all radar systems used to compose this radiostratigraphy are sufficiently well calibrated radiometrically. Therefore, radar data are analyzed only if the campaign during which it was collected is radiometrically stable.

Data collected prior to 2003 had a manually controlled analog gain applied during collection, and changes in this gain were recorded only intermittently [*Chuah*, 1997; *Gogineni et al.,* 1998]. This gain varies as a function of traveltime, preventing meaningful echo-intensity analysis within a given trace, so we ignore those data here. For some later campaigns, additional unresolved issues in radiometric calibration prevent direct interpretation of P_r. Hence, in this study we consider data from five campaigns only, collected using two aircraft: 2003 (P3-B Orion; P3), 2008 (DHC-6 Twin Otter; TO), 2011, 2012, and 2013 (P3) (Figure 1). Three radar systems were used in these campaigns: (1) Advanced Coherent Radar Depth Sounder (ACORDS; 150 MHz center frequency; 2003), (2) Multi-Channel Radar Depth Sounder (MCRDS; 150 MHz; 2008), and (3) Multi-Channel Coherent Radar Depth Sounder (MCoRDS; 195 MHz; 2011–2013). Within these campaigns, two transects with unresolved calibration issues were also ignored.

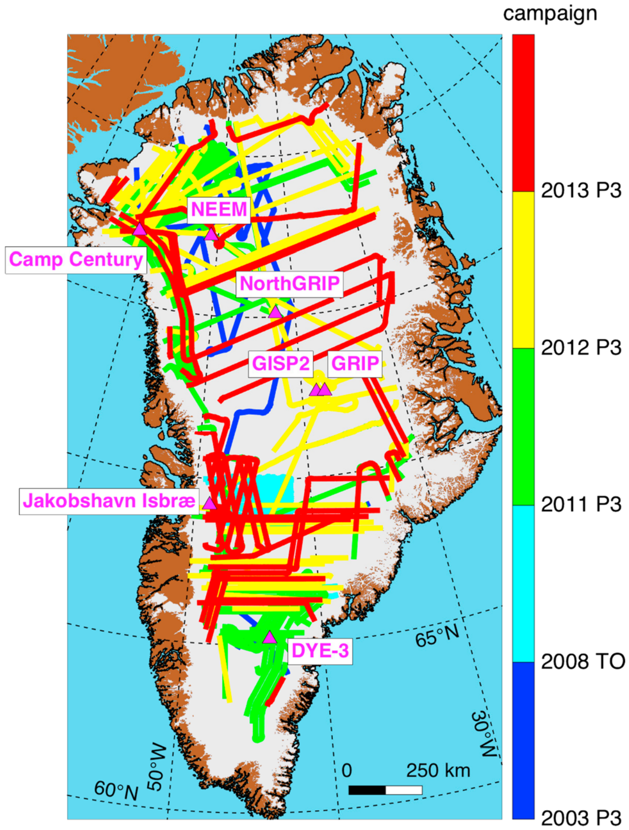

Figure 1. KU airborne ice-penetrating radar surveys collected over the GrIS used in this study and locations of deep boreholes with temperature profiles.

A critical concern in the analysis of P_r is its relationship with reflection slope. Through several mechanisms, nonnegligible slopes can decrease P_r, and we evaluate the set of potential slope-dependent power-loss mechanisms described by *Holschuh et al.* [2014]. For the KU data considered here, reflection slopes are typically less than 1°, but slopes up to ~10° were traced. The effective horizontal interval for coherent along-track stacking is between one quarter and one half of the englacial wavelength, equivalent to 0.21–0.56 m; therefore, we ignore potential power loss due to destructive stacking. We ignore the relatively small effect of changing path length on the echo intensity of Doppler-binned internal reflections prior to SAR focusing. For the half-wavelength dipoles of the radar systems we used, the theoretical 3 dB beamwidth in the along-track direction is ~115°. Because of the ground-plane effect of the aircraft wings, the effective beamwidth is narrower but still much larger than the Doppler beamwidth (≲10°); therefore, we do not correct for antenna directivity. Due to windowing in the Doppler domain prior to coherent migration, SAR focusing induces slope-dependent power loss. To correct for this effect, we adjust reflection slopes for air-ice refraction (ignoring firn) and surface slope to determine the Doppler angle of each reflection and the appropriate correction for P_r. We limit the magnitude of this correction to 10 dB (otherwise the P_r value is discarded) and restrict permissible reflections to those with Doppler angles less than or equal to 4°, equivalent to an englacial reflection slope of 2.25°, assuming a horizontal ice surface.

2.2. Ice-Core and Borehole Data

To model radar attenuation, knowledge of the englacial concentration of several key impurities is required. For this purpose, we use the depth profile of soluble ions within the Greenland Ice Core Project (GRIP) ice core [*Legrand and de Angelis*, 1996], as it is the most complete record of such ions from the Greenland deep ice cores and one of the high-frequency-limit conductivity models that we use later on was determined empirically using the major ion records from this ice core [*Moore et al.*, 1994; *Wolff et al.*, 1997]. We calculate ice acidity using the charge-balance method and all measured ions [e.g., *MacGregor et al.*, 2007].

Table 1. Borehole-Temperature Profiles Used to Evaluate Relationship Between Radar-Attenuation Rate and Ice Temperature

Borehole	Ice Thickness (m)	Temperature Data Reference
Camp Century	1380	*Weertman* [1968]
DYE-3	2037	*Gundestrup and Hansen* [1984]
GISP2	3053	*Cuffey et al.* [1995]
GRIP	3029	*Dahl-Jensen et al.* [1998]
NEEM	2561	This study
NorthGRIP	3085	*Dahl-Jensen et al.* [2003]

Quantitative evaluation of radar-inferred temperature requires knowledge of in situ temperature. For this purpose, we use the temperature-depth profiles measured in six deep boreholes across the GrIS (Table 1 and Figure 1). Five of these profiles are available from earlier studies, and the temperature-depth profile at the North Greenland Eemian (NEEM) borehole was measured and processed using established techniques [*Clow et al.,* 1996; *Clow,* 2008, 2014]. Additional full-thickness borehole-temperature profiles exist for the GrIS within and near Jakobshavn Isbræ and Isunnguata Sermia. [*Lüthi et al.,* 2002, 2015; *Harrington et al.,* 2015]. We compare three borehole-temperature profiles collected and summarized by *Lüthi et al.* [2002] ~50 km upstream of Jakobshavn Isbræ's terminus (Figure 1) to nearby radar-inferred temperatures, but those boreholes were not directly overflown by the radar transects used in this study, so these data are not used to quantitatively evaluate radar-inferred temperature. The more recent boreholes measured by *Lüthi et al.* [2015] and *Harrington et al.* [2015] are too distant from radar inferences of temperature to be considered in this study.

To model the radar reflectivity within the GrIS and evaluate a key assumption regarding the method for estimating radar attenuation, we use the dielectric profiles (DEP) of the GRIP, NorthGRIP, and NEEM ice cores [*Wolff et al.,* 1997; *Rasmussen et al.,* 2013].

2.3. Ice-Sheet Temperature Model

To evaluate radar-inferred englacial temperature across the GrIS, a model of ice-sheet temperature is required. This need is especially acute because sparse boreholes are located mostly along ice divides, where horizontal advection of heat is expected to be low and likely to have been so for at least several millennia. Here we use the temperature output from a steady state, three-dimensional (3-D) thermomechanical model of the GrIS described by *Seroussi et al.* [2013]. This model is an instance of the Ice Sheet System Model (ISSM) that uses the SeaRISE data sets for several boundary conditions [*Nowicki et al.,* 2013]. The stress balance includes higher-order terms when calculating ice flow, and basal friction is inferred by minimizing the misfit between modeled and observed surface velocities using inverse methods. The thermal regime is based on an enthalpy formulation [*Aschwanden et al.,* 2012] and assumes thermal steady state. This model therefore does not account directly for the past climate history of the GrIS, which is known to have varied substantially [e.g., *Cuffey et al.,* 1995; *Cuffey and Clow*, 1997; *Dahl-Jensen et al.,* 1998], nor other processes affecting ice-sheet temperature that may be more important closer to the ice-sheet margin, such as cryohydrologic warming [*Lüthi et al.,* 2015]. Because this model does not consider the surface-temperature or accumulation-rate history of the GrIS, differences between its temperature output and radar-inferred temperatures can potentially indicate differences between modern and past boundary conditions.

For an initial guess for the radar-inferred temperature in our iterative misfit minimization scheme (equation (8)), we use the mean annual surface-temperature field from the SeaRISE data sets [*Ettema et al.,* 2009; *Nowicki et al.,* 2013]. This surface-temperature field is the same as the surface boundary condition for temperature used by *Seroussi et al.* [2013].

3. Methods

3.1. Radar-Attenuation Rate From Internal Reflections

We determine the depth-averaged rate of power loss due to englacial radar attenuation $\overline{N}_a$ (dielectric absorption by the ice column) following a modification of the method described by *Matsuoka et al.* [2010b]. A key advantage of this method is that it does not rely on the bed reflection to estimate $\overline{N}_a$, because that reflector is inherently more complex and known to be spatially variable except within limited regions [e.g., *Winebrenner et al.,* 2003; *Schroeder et al.,* 2013]. It is therefore not appropriate to assume that the bed reflectivity is uniform across the entire GrIS for the purpose of calculating $\overline{N}_a$. The chosen method does not require the assumption that the radar reflectivity R of internal reflections is horizontally uniform, which is unlikely to be valid across a whole ice sheet, particularly for reflections of volcanic origin that do occur within ice sheets [*Hempel et al.,* 2000; *Jacobel and Welch*, 2005; *Corr and Vaughan*, 2008]. The primary disadvantage of this method is that numerous internal reflections must be traced to reliably constrain $\overline{N}_a$, a problem that is addressed here by the use of the extensive GrIS radiostratigraphy described by *MacGregor et al.* [2015]. A further disadvantage is that by relying on traced internal reflections only, this method cannot sample the entire ice column.

We assume that all internal reflections are specular, as expressed in the processed KU radar data, and that R is vertically uniform. The specularity assumption is well supported by observations of the along-track coherence of most internal reflections and their behavior as a function of angle of incidence [*Drews et al.,* 2009; *Holschuh et al.,* 2014; *MacGregor et al.,* 2015]. The assumption of vertically uniform reflectivity is less ideal, as there are several distinct and remarkably radar-bright reflections that date to the Last Glacial Period (LGP) within the

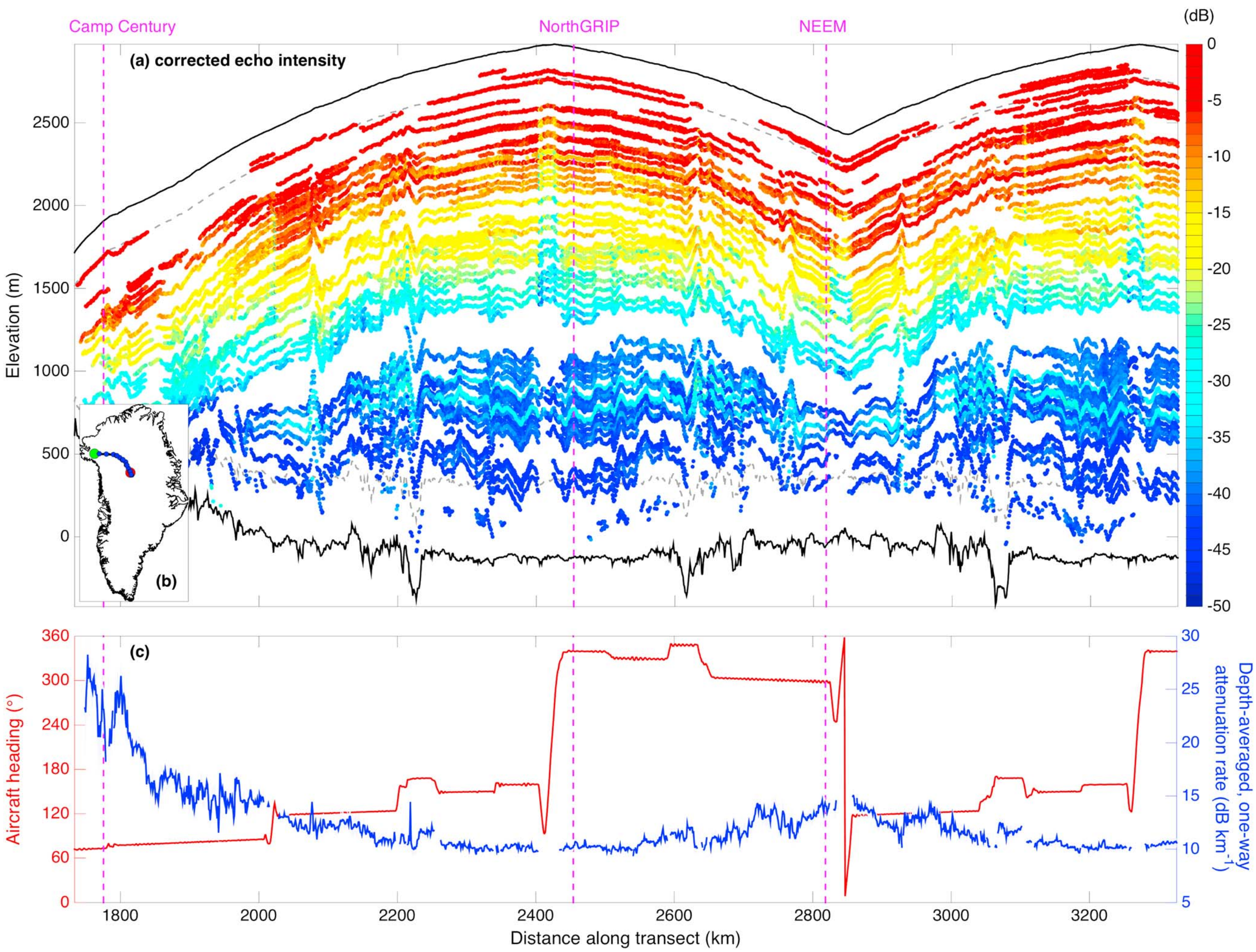

Figure 2. (a) Geometrically and slope-corrected echo intensities ([P_{rc}]) recorded by a single transect (6 May 2011; MCoRDS on P3). Surface and bed reflections are shown as black solid lines. This transect's closest intersections with three ice cores (within 5 km) are shown as vertical magenta dashed lines. Upper (200 m) and lower (0.85 *H*) depth bounds are shown as gray dashed lines. (b) Location of transect across the GrIS (green/red circles: start/end of transect; blue circles: 100 km intervals). (c) Aircraft heading (red) and depth-averaged radar-attenuation rate ($\overline{N}_a$; blue) estimated using [P_{rc}] shown in Figure 1a. Light blue shading represents $\overline{N}_a \pm \widetilde{N}_a$. $\overline{N}_a$ is not calculated where the absolute change in aircraft heading exceeds 2° km^{-1}.

GrIS [*NEEM community members*, 2013; *MacGregor et al.,* 2015] (Figure 2a). However, apparent radar reflectivity is more vertically uniform within the portion of the GrIS that was formed since the beginning of the Bølling/Allerød period 14.7 ka ago [*Karlsson et al.,* 2013; *MacGregor et al.,* 2015], where the majority of reflections were traced. Further, an analysis of DEP profiles shows that the assumption of uniform R is reasonable for the purpose of estimating $\overline{N}_a$ (Appendix A).

We first bin P_r horizontally for all traced reflections into 1 km segments along-track. This segment length is at least an order of magnitude larger than the diameter of the first Fresnel zone for these reflections but of the same order as the length scales used by *Matsuoka et al.* [2010b]. We average each reflection's along-track-binned P_r values between their 70$^{\text{th}}$ and 95$^{\text{th}}$ percentiles, but we do not bin reflections by depth. For specular internal reflections, the slope-corrected observed echo intensity P_r^i from the i th reflection is

$$P_r^i = P_t \left(\frac{\lambda_{\text{air}}}{4\pi}\right)^2 \frac{G_a^2 T^2 \left(L_a^i\right)^2 L_{vs} L_b L_{\text{sys}} G_p R}{4\left(h + \frac{z_i}{\sqrt{\varepsilon'_{\text{ice}}}}\right)^2}, \tag{1}$$

where P_t is the transmitted power, λ_{air} is the radar wavelength in air, G_a is the antenna gain, T is the transmission loss at the air-ice interface, L_a is the one-way loss due to attenuation, L_{vs} is the total loss due to volume scattering, L_b is the total loss due to englacial birefringence, L_{sys} is the total system loss, G_p is the processing gain, h is the height of the aircraft above the ice surface, z is depth, and $\varepsilon_{ice}^{'}$ is the real part of the complex relative permittivity of ice (assumed to be 3.15). The geometrically corrected echo-intensity P_{rc}^{i} of the i th reflection is (e.g., Figure 2a)

$$P_{rc}^{i} = P_{r}^{i}\left(h + \frac{z_i}{\sqrt{\varepsilon_{\mathrm{ice}}^{'}}}\right)^2. \tag{2}$$

The exponent in equations (1) and (2) associated with power loss due to geometric spreading implicitly assumes that the internal reflections are specular. P_t, λ_{air}, G_a, T, L_{sys}, G_p, and $\varepsilon_{\mathrm{ice}}^{'}$ are assumed to be invariant for any given radar trace; i.e., they may vary horizontally but not within a single recorded trace [*Matsuoka et al.,* 2010b]. Poorly constrained G_p in earlier KU data is the principal factor preventing use of those data in this study. Following *Paden et al.* [2005] and *Matsuoka et al.* [2010b], we assume that L_{vs} and L_b are negligible.

Based on the assumption of invariance for most of the terms in equation (1), the ratio of P_{rc}^{i} to that of the first observed reflection ($i = 0$) is

$$\frac{P_{rc}^{i}}{P_{rc}^{0}} = \left(\frac{L_a^i}{L_a^0}\right)^2. \tag{3}$$

In units of decibels (represented by square brackets), equation (3) becomes

$$\begin{aligned} \left[P_{rc}^{i}\right] - \left[P_{rc}^{0}\right] &= 2\left(\left[L_a^i\right] - \left[L_a^0\right]\right), \\ \Delta\left[P_{rc}^{i}\right] &= 2\Delta\left[L_a^i\right], \end{aligned} \tag{4}$$

where $\Delta\left[P_{rc}^{i}\right]$ is the difference in $[P_{rc}]$ between the first and ith observed reflections and $\Delta\left[L_a^i\right]$ is the total one-way attenuation within the portion of the ice column between those two reflections. The total attenuation to the ith reflection is related to $\overline{N}_a$ as

$$\Delta\left[P_{rc}^{i}\right] = -2\overline{N}_a\left(\sum_{j=1}^{i}\Delta z_j\right) + b, \tag{5}$$

where $\Delta z_j = z_j - z_{j-1}$ and b is a correction factor. In this formulation and $\overline{N}_a$ is a positive quantity following earlier convention and a one-way rate [e.g., *MacGregor et al.,* 2007]. It is determined using a weighted linear least-squares fit to equation (5) whose weights are $\left[\widetilde{P}_{rc}^{i}\right]^{-2}$, where $\left[\widetilde{P}_{rc}^{i}\right]$ is the standard deviation of $\left[P_{rc}^{i}\right]$ within the 1 km segment. Following this approach, b is a zero-intercept best-fit value for equation (5)'s linear relationship that effectively acknowledges that $\left[P_{rc}^{0}\right]$ is not perfectly known. We found that explicitly setting $b = 0$ resulted in noisier along-track profiles of $\overline{N}_a$. This approach also returns $\tilde{N}_a$, the standard error for $\overline{N}_a$.

We constrain the calculation of $\overline{N}_a$ as follows:

1. P_{rc} decreases during aircraft maneuvers due to the nonnegligible aircraft roll and consequent off-nadir pointing of the mounted antennae (e.g., Figure 2). Changing aircraft roll results in changing effective reflection slope, so roll-dependent power loss is analogous to that of the slope-dependent power loss discussed above. Because aircraft-roll data are not available for all campaigns, rather than correct for this effect directly, we ignore 1 km segments of a transect where the aircraft heading differs by more than 2° from that of the previous 1 km segment.
2. At least five internal reflections are required to calculate $\overline{N}_a$, including the shallowest reflection used to normalize the deeper reflections.
3. The depth of the shallowest reflection z_{min} must be greater than or equal to 200 m, to avoid complications associated with the firn column, following *Matsuoka et al.* [2010b].
4. The depth of the deepest reflection z_{max} must be less than or equal to 0.85 H, where H is ice thickness, so that very deep reflections with low signal-to-noise ratios do not bias $\overline{N}_a$.
5. The thickness of the column h between z_{min} and z_{max} must be greater than or equal to 0.25 H.

Following the nomenclature of *Matsuoka et al.* [2010b], we are effectively assuming that all reflections used to calculate $\overline{N}_a$ are bright and that the depth gradient of R is negligible, so that equation (5) constrains $\overline{N}_a$ in a manner comparable to that of the upper envelope gradient. *Jacobel et al.* [2010] applied a similar method to internal reflections recorded by a ground-based survey in East Antarctica and reported good agreement between $\overline{N}_a$ values calculated using either the brightest reflections only or all traced reflections, supporting our approach. Separate experiments (not shown) using an averaged P_r (rather than the 70th–95th percentiles) and/or longer along-track binning do not change the results significantly.

In taking the above approach, we must assume that $\overline{N}_a$ is vertically uniform within the portion of the ice column bounded by z_{min} and z_{max}. This assumption is unlikely to be valid at small vertical scales (< ~10 m) but may be acceptable at scales greater than 100 m in isothermal ice that does not include a glacial-interglacial transition, because temperature is the dominant control on $\overline{N}_a$ at larger vertical scales [*MacGregor et al.,* 2007]. At or near a GrIS ice divide, the top ~50–75% of the ice column is typically isothermal and close to the mean annual surface temperature T_s [*Cuffey and Paterson*, 2010]. The proportion of ice column that is isothermal is expected to decrease away from ice divides, due to increasing basal friction, increasing rates of shear deformation and increasing horizontal advection of heat. Also, the portion of the ice column where *MacGregor et al.* [2015] traced and dated internal reflections typically includes the transition between the Holocene and the LGP, except in southern Greenland, where this transition is harder to detect and closer to the bed. These considerations do not preclude the calculation of $\overline{N}_a$, but they do imply that depth-averaged values may mask substantial depth variability in N_a. Hence, while we report $\overline{N}_a$ only, we emphasize that these values do not necessarily indicate that radar-attenuation rates are vertically uniform within the sampled portion of the ice sheet. Rather, reported values of $\overline{N}_a$ represent a first widespread, depth-averaged constraint on radar attenuation rates within the GrIS from these data.

3.2. Temperature From Radar-Attenuation Rate

In low-loss dielectrics such as ice, N_a in dB km^{-1} is proportional to the high-frequency-limit (HF-limit) electrical conductivity σ_∞ in μS m^{-1} as [*MacGregor et al.,* 2007, 2012]

$$N_a = \frac{10\log_{10}e}{1000\varepsilon_0\sqrt{\varepsilon'_{\text{ice}}}c}\sigma_\infty, \tag{6}$$

where ε_0 is the permittivity of the vacuum and c is the speed of light in the vacuum. Because σ_∞ is known to be both temperature and impurity dependent, a σ_∞ model with these dependencies is required to relate $\overline{N}_a$ to the temperature of the ice column. Because $z_{min} \geq 200$ m and hence deeper than the expected firn thickness, we ignore the density dependence of the radar-attenuation rate [*MacGregor et al.,* 2012]. We assume initially that ice conductivity σ is frequency-independent between the medium frequency (MF; 0.3–3 MHz) range and the very high frequency (VHF; 30–300 MHz) range, i.e., $\sigma = \sigma_\infty$. This range bounds the operating frequencies of the KU radar systems used in this study.

A common form of suitable σ_∞ models for ice assumes an Arrhenius-form temperature dependence, a linear dependence on the concentration of certain lattice-soluble impurities and that the temperature dependence (activation energy) varies depending on the nature of the conductivity contribution [e.g., *MacGregor et al.,* 2007]:

$$\begin{aligned}\sigma_\infty = {} & \sigma_{\text{pure}}\exp\left[\frac{E_{\text{pure}}}{k}\left(\frac{1}{T_r}-\frac{1}{T}\right)\right] \\ & + \mu_{\text{H}^+}[\text{H}^+]\exp\left[\frac{E_{\text{H}^+}}{k}\left(\frac{1}{T_r}-\frac{1}{T}\right)\right] \\ & + \mu_{\text{Cl}^-}[\text{Cl}^-]\exp\left[\frac{E_{\text{Cl}^-}}{k}\left(\frac{1}{T_r}-\frac{1}{T}\right)\right] \\ & + \mu_{\text{NH}_4^+}\left[\text{NH}_4^+\right]\exp\left[\frac{E_{\text{NH}_4^+}}{k}\left(\frac{1}{T_r}-\frac{1}{T}\right)\right],\end{aligned} \tag{7}$$

where k is the Boltzmann constant, T is temperature, T_r is a reference temperature, and [H^+], [Cl^-], and [NH_4^+] are molarities for those respective impurities. The magnitudes of these dependencies are represented by the values of eight dielectric properties: the pure ice conductivity σ_{pure}, its activation energy E_{pure}, and the molar conductivities μ and activation energies of the acid (H^+), chloride (Cl^-), and ammonium (NH_4^+) contributions to σ_∞. We initially consider two existing σ_∞ models (M07 and W97), which are described in detail in Appendix B. The values of the HF-limit dielectric properties used in these models are given in Table 2.

Table 2. Values of the High-Frequency Dielectric Properties of Ice Used in the Conductivity Models

Symbol	Description	Units	W97[a]	M07[a]
T_r	Reference temperature	°C	−15	−21
σ_{pure}	Conductivity of pure ice	$\mu S\ m^{-1}$	9	9.2 ± 0.2
μ_{H^+}	Molar conductivity of H^+	$S\ m^{-1}\ M^{-1}$	4	3.2 ± 0.5
μ_{Cl^-}	Molar conductivity of Cl^-	$S\ m^{-1}\ M^{-1}$	0.55	0.43 ± 0.07
$\mu_{NH_4^+}$	Molar conductivity of NH_4^+	$S\ m^{-1}\ M^{-1}$	1	0.8[b]
E_{pure}	Activation energy of pure ice	eV	0.58[c]	0.51 ± 0.01
E_{H^+}	Activation energy of H^+	eV	0.21[c]	0.20 ± 0.04
E_{Cl^-}	Activation energy of Cl^-	eV	0.23[c,d]	0.19 ± 0.02
$E_{NH_4^+}$	Activation energy of NH_4^+	eV	0.23[c]	0.23[c]

[a]W97: *Wolff et al.* [1997] relationship between DEP-measured σ_∞ and soluble chemistry for the GRIP ice core (equation (B1)). M07: *MacGregor et al.* [2007] adjusted using pure-ice dielectric properties reported by *Johari and Charette* [1975] and using the same the dielectric properties for NH_4^+ as W97.
[b]Value corrected from −15 °C to −21 °C using the assumed activation energy for the W97 model.
[c]Activation energies selected assuming only impurities that form lattice defects contribute to σ_∞, following *Stillman et al.* [2013a, Table 1].
[d]Sea-salt Cl^-, as described by *MacGregor et al.* [2007], is assumed to represent extrinsic Bjerrum L-defects formed by lattice-partitioned Cl^- [*Stillman et al.*, 2013a].

Figure 3 shows the range of these two σ_∞ models as a function of temperature and chemistry. Using the mean impurity concentrations during the both the Holocene epoch (0–11.7 ka; 1.6 ± 1.2, 0.4 ± 0.4, and 0.5 ± 0.6 μM for [H^+], [Cl^-] and [NH_4^+], respectively) and the LGP (11.7–115 ka; 0.2 ± 0.5, 1.8 ± 1.0, and 0.4 ± 0.4 μM), it is clear that attenuation rates are consistently predicted to be lower during the LGP. Model W97 predicts lower radar-attenuation rates for all temperatures as compared to model M07 (~65% of M07). Across the likely temperature range for the GrIS, radar-attenuation rates are related nonlinearly to ice temperature. Thus, the radar-attenuation rate is more sensitive to temperature at higher temperatures. The ranges of impurity concentrations during both the Holocene and the LGP are sufficiently large that they may confound inference of englacial temperature from $\overline{N}_a$. Thus, we expect that the effect of spatially varying chemistry on radar attenuation will be greater for the GrIS than that previously modeled for the Vostok flowline in East Antarctica [*MacGregor et al.*, 2012].

We use the isochrone ages determined by *MacGregor et al.* [2015] to vertically rescale the GRIP impurity-concentration profiles across the GrIS, assuming that all impurities are wet-deposited only [*MacGregor et al.*, 2012]. *Alley et al.* [1995] found that at GISP2, soluble ion fluxes were consistent with a primary contribution from wet deposition (>80%) during both warm and cold periods following the Last Glacial Maximum. The proportion of an impurity that is wet-deposited increases with increasing accumulation rate, so each impurity's wet-deposited proportion is likely higher across the majority of the GrIS except in northeastern Greenland, where accumulation rates tend to be lower than at GISP2 [*Ettema et al.*, 2009].

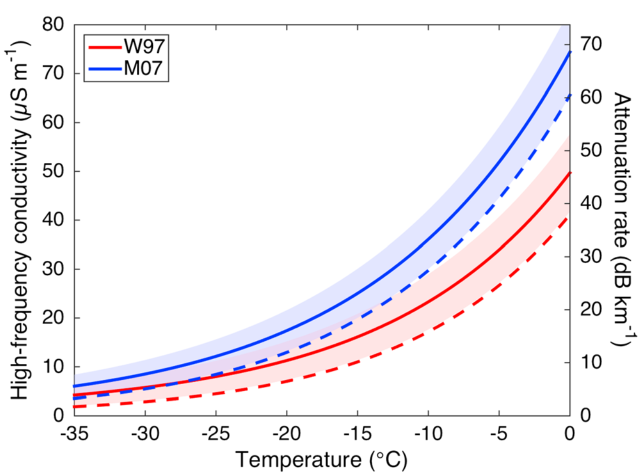

Figure 3. HF-limit ice conductivity σ_∞ as a function of the likely temperature range of the GrIS, using two different σ_∞ models (Table 2). Solid lines and shading (uncertainty) are calculated using the mean and standard deviation of impurity concentrations during the Holocene from the GRIP ice core. Dashed lines are calculated using mean LGP impurity concentrations.

For both σ_∞ models, we determine the depth-averaged englacial temperature $\overline{T}_a$ that minimizes the χ^2 residual between the observed and modeled depth-averaged radar-attenuation rates as

$$\chi^2 = \frac{\left[\overline{N}_a - \frac{1}{h}\sum_{i=1}^{n-1} N_a^i \Delta z_i\right]^2}{\widetilde{N}_a^2}, \quad (8)$$

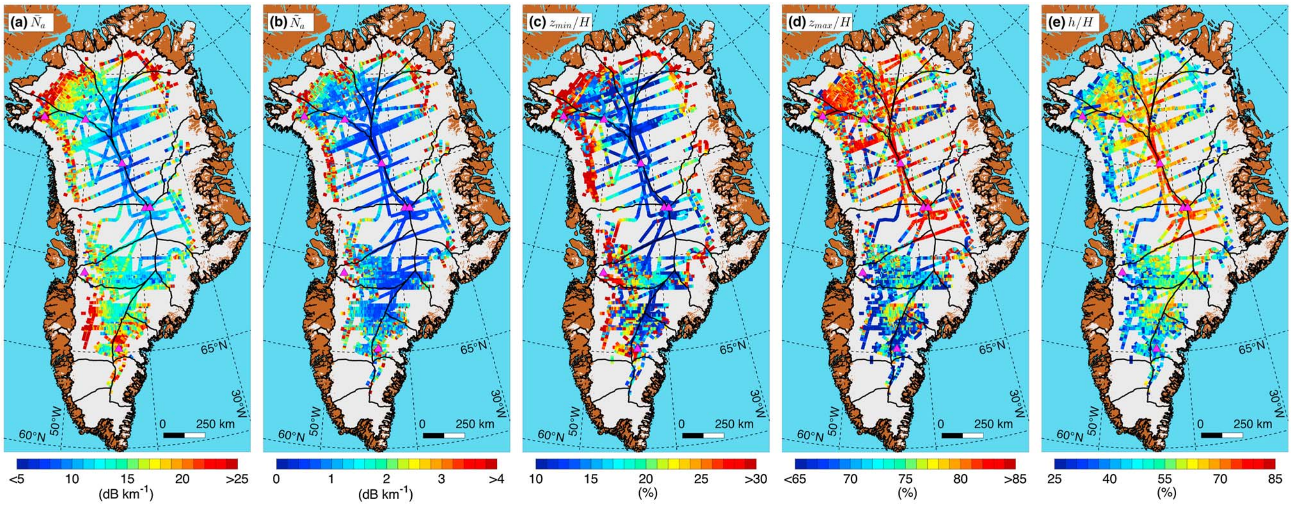

Figure 4. (a, b) Radar-inferred depth-averaged attenuation rate ($\overline{N}_a$) and its uncertainty ($\tilde{N}_a$) across the GrIS, respectively. (c, d) Ice-thickness-normalized depths of shallowest and deepest reflections used to infer $\overline{N}_a$, i.e., z_{min}/H and z_{max}/H, respectively. (e) Fraction of ice thickness sampled to determine $\overline{N}_a$ (h/H).

where n is the number of observed reflections and N_a^i is the modeled radar-attenuation rate within the ith depth interval using $\overline{T}_a$ and the vertically rescaled GRIP impurity-concentration profiles. This formulation permits estimation of confidence bounds for $\overline{T}_a$ using $\Delta\chi^2$ distributions, which we difference from $\overline{T}_a$ and average to estimate $\widetilde{T}_a$, the standard error in $\overline{T}_a$. We note that uncertainties in the dielectric properties that form the σ_∞ models (Table 1) are not directly incorporated into $\widetilde{T}_a$. The initial guess for $\overline{T}_a$ is the mean annual surface temperature $\overline{T}_s$.

As for $\overline{N}_a$, the inference of $\overline{T}_a$ between z_{min} and z_{max} assumes that the ice sheet is isothermal within this depth range [*Matsuoka et al.*, 2010b]. If true, such a scenario simplifies interpretation of $\overline{T}_a$, but it is difficult to verify across the entire GrIS. Rather, $\overline{T}_a$ is assumed to represent the depth-averaged englacial temperature within this depth range, which may mask substantial englacial temperature variability that we cannot resolve using this method.

4. Results

4.1. Radar-Attenuation Rate

We find large spatial variation in $\overline{N}_a$ across the GrIS (Figure 4a), exceeding its formal uncertainty range even along the central ice divide (Figure 4b). Values range between less than 10 dB km^{-1} along the central ice divide to greater than 25 dB km^{-1} within ~100 km of the ice-sheet margin. Across most of the GrIS, $\tilde{N}_a$ is less than 1 dB km^{-1} (Figure 4b). We note that this uncertainty accounts directly for uncertainty in [P_{rc}] only and not any other factors that may influence estimation of $\overline{N}_a$ but which are harder to quantify.

The depth of the shallowest reflection used (Figure 4c) varied more than that of the deepest reflection used (Figure 4d). Toward the ice-sheet margin, the depths of the shallowest and deepest reflections used tend to converge, due to ice flow and the challenge of tracing reflections there [*MacGregor et al.*, 2015]. We typically sampled more than 70% of the ice thickness within the ice-sheet interior and more than 40% across most of the GrIS (Figure 4e).

At the 711 transect intersections (cross-overs), the differences between values of $\overline{N}_a$ are normally distributed (Figure 5), with a Gaussian-best-fit cross-over difference of -0.3 ± 3.2 dB km^{-1}. The small bias from zero suggests that the method is sampling the same physical property of the ice column, regardless of aircraft heading or transect used; i.e., our estimates of $\overline{N}_a$ may incorporate effects other than dielectric attenuation (e.g., volume scattering or birefringence), but these effects must also be smoothly varying. The relatively large cross-over standard deviation indicates the underlying uncertainty in estimating $\overline{N}_a$ using internal reflections that is not accounted for by $\tilde{N}_a$.

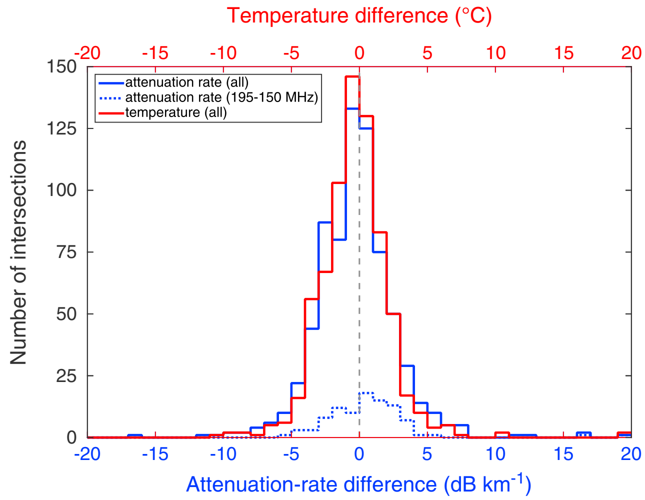

Figure 5. Difference between values of $\overline{N}_a$ (blue) and $\overline{T}_a'$ (red) at transect intersections. An intersection is only included in this comparison if both z_{min} and z_{max} values for each transect are within 0.05 H of each other, respectively. For the $\overline{N}_a$ difference labeled in the legend as "attenuation rate (195–150 MHz)" (blue dotted line), only intersections between transects collected at the two different frequencies are considered, and a positive (negative) difference indicates a greater (smaller) $\overline{N}_a$ value at 195 MHz.

For the 94 cross-overs between data from the first two campaigns (2003/2008; 150 MHz center frequency) and the three subsequent campaigns (2011/2012/2013; 195 MHz center frequency), the mean difference in $\overline{N}_a$ is 0.7 ± 3.5 dB km^{-1} between these campaigns, where a positive difference indicates greater $\overline{N}_a$ values at 195 MHz (Figure 5). Relative the mean cross-over value of $\overline{N}_a$ at each intersection, this difference is equivalent to $5 \pm 24\%$ of $\overline{N}_a$. However, this difference is not significantly different from zero ($p = 0.42$).

These observations show clearly that englacial radar attenuation varies across GrIS in a manner similar to model predictions for the West Antarctic Ice Sheet [*Matsuoka et al.*, 2012]. The spatial variability in $\overline{N}_a$ is muted compared to the horizontal gradients in those full-thickness predictions of $\overline{N}_a$, likely because our method does not sample the highest temperatures in the ice column near the bed, where depth-averaged attenuation rates can increase substantially [*MacGregor et al.*, 2007].

4.2. Radar-Inferred Temperature

We first compare $\overline{T}_a$ values inferred using both σ_∞ models where transects intersect boreholes (Figure 6). We consider a transect to have intersected a borehole if it passes within a 5 km radius of the borehole. This radius is larger than that used by *MacGregor et al.* [2015] (3 km), because we assume that the horizontal spatial variation in englacial temperature is smaller than that of age. Note that this threshold is not met by the *Lüthi et al.* [2002] boreholes, for which the closest radar-inferred temperature was ~30 km away. Hence, only the deep interior boreholes are used to quantitatively evaluate $\overline{T}_a$.

Model W97 overestimates borehole-measured temperature more than M07. The difference between either model's values of $\overline{T}_a$ and the depth-averaged borehole temperatures ($\overline{T}_b$) can be expressed as a temperature difference ΔT_c:

$$\overline{T}_b = \overline{T}_a + \Delta T_c \tag{9}$$

We calculate the best-fit value of ΔT_c, accounting for both $\widetilde{T}_a$ and the standard deviation of the borehole-measured temperature within the equivalent depth range. For Model W97, $\Delta T_c = -13.0 \pm 3.3$ K, and for M07, $\Delta T_c = -6.8 \pm 3.3$ K.

Although the range of $\overline{T}_a$ for either model at an individual borehole can be large (>5 K for Camp Century), the interborehole relationships between $\overline{T}_a$ are clearer and more self-consistent. For these six boreholes, the range of temperatures within the sampled depth range is ~15 K. Although $\overline{T}_a$ is often a poor representation of the absolute englacial temperature, these patterns confirm that the temperature dependence of both σ_∞ models is reasonable and that the relative spatial variation in $\overline{T}_a$ is indeed related to englacial temperature.

Both σ_∞ models predict temperatures that are too high compared to that measured in boreholes, suggesting that they do not account for a significant loss mechanism. We hypothesize that this mechanism is the frequency dependence of σ between MF and VHF. Although we observed a small frequency dependence in $\overline{N}_a$, it was not significant. In Appendix C, we further evaluate this frequency dependence using recent broadband measurements of ice cores [*Stillman et al.*, 2013a] and inferences from existing radar experiments. This analysis indicates that σ is indeed frequency-dependent between MF and VHF, which justifies a

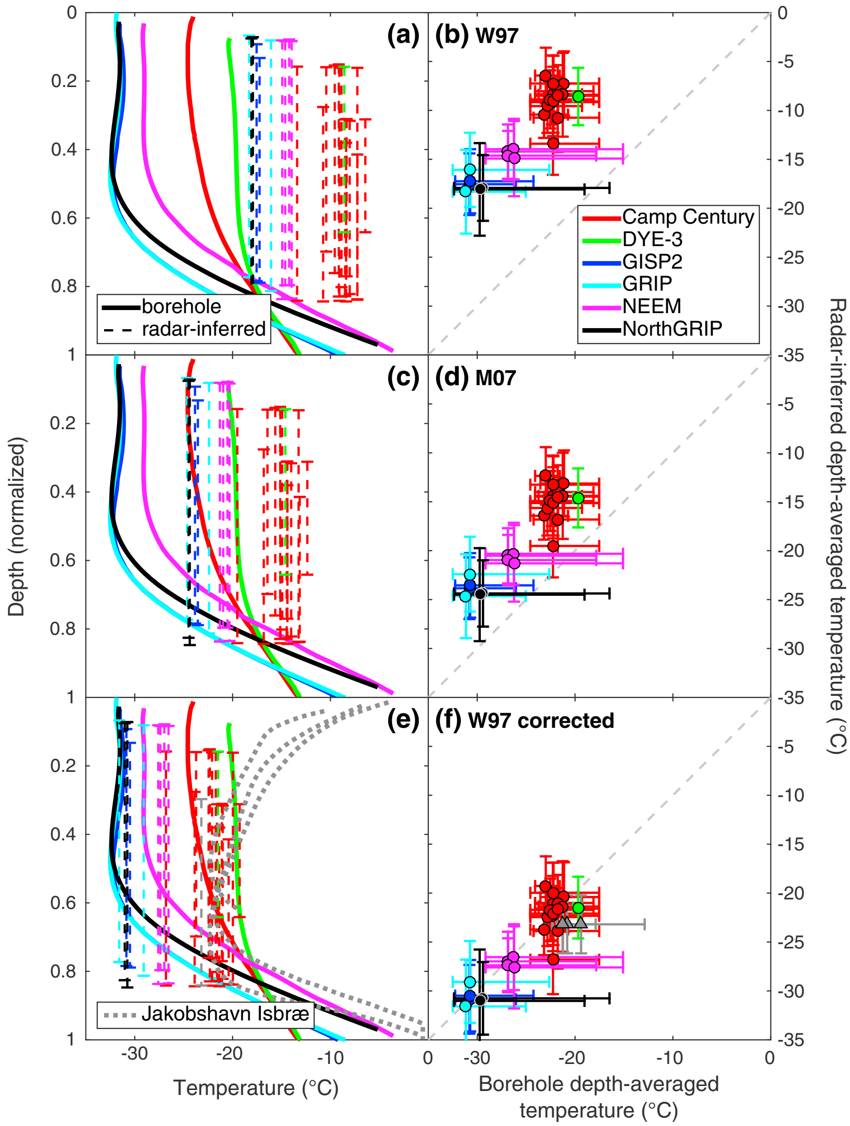

Figure 6. (a, c, e) Borehole-measured and radar-inferred temperature profiles for the six deep ice cores recovered from the GrIS, normalized by the local ice thickness, for two different σ_∞ models (Table 2) and the corrected W97 model. Solid lines are the borehole-measured profiles (Table 1), and the vertical dashed lines represent the radar-inferred values of $\overline{T}_a$ between each transect's values of z_{min} and z_{max}. (b, d, f) Relationships between the depth-averaged borehole-measured temperature $\overline{T}_b$ (between z_{min} and z_{max}) and $\overline{T}_a$ ($\overline{T}_a'$ for Figure 6f). Horizontal bounds indicate the range of borehole temperatures measured between z_{min} and z_{max}, while vertical bounds represent $\overline{T}_a \pm \widetilde{T}_a$ ($\overline{T}_a' \pm \widetilde{T}_a'$ for Figure 6f).

correction to reconcile $\overline{T}_a$ and $\overline{T}_b$. Given this physical basis for the difference between $\overline{T}_a$ and $\overline{T}_b$, we correct $\overline{T}_a$ by adjusting the σ_∞ models directly, rather than correcting $\overline{T}_a$ using ΔT_c.

Only model W97 is referenced to a specific frequency (300 kHz). It is therefore the only σ_∞ model that can be corrected directly for frequency dependence, and it is the only model that we consider hereafter. We determine the best-fit factor β for σ_∞ that is necessary to minimize the difference between $\overline{T}_a$ and $\overline{T}_b$, taking into account the reference frequency of model W97 (300 kHz) and the center frequency of the radar system for each transect-borehole intersection (either 150 or 195 MHz). For these 25 radar-borehole intersections, $\beta = 2.6 \pm 0.3$ between 300 kHz and 150–195 MHz, which is equivalent to a depth-averaged Cole-Cole distribution parameter ($\overline{\alpha}$) of 0.15 ± 0.02 (Appendix C). This value of $\overline{\alpha}$ implies that the mean relative difference for $\overline{N}_a$ between 150 and 195 MHz will be ~4% (Appendix C), which is a small effect but comparable to that which we observed (5 ± 24%).

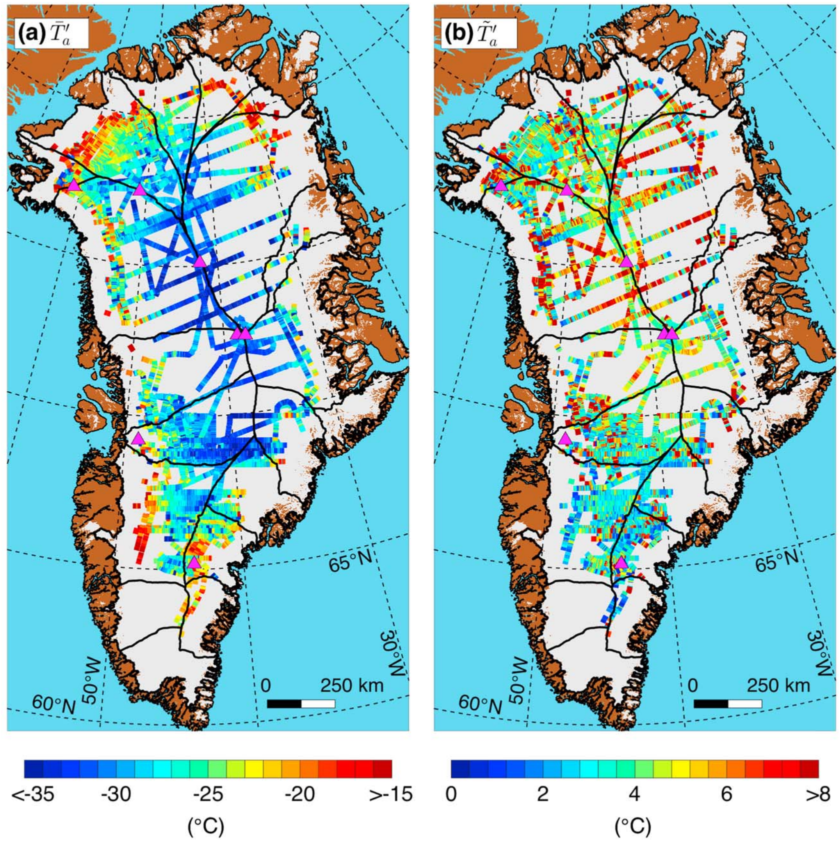

Figure 7. (a, b) Corrected radar-inferred depth-averaged temperature ($\overline{T}'_a$) and its uncertainty ($\widetilde{T}'_a$) across the GrIS, respectively.

We correct model W97 using β and calculate the corrected depth-averaged temperature $\overline{T}'_a$ and its uncertainty $\widetilde{T}'_a$. Figure 6f shows the relationship between $\overline{T}'_a$ and $\overline{T}_b$. For this relationship, the fraction of explained variance (r^2) is 0.85 for a weighted linear regression that accounts for both $\widetilde{T}'_a$ and a nominal uniform uncertainty for $\overline{T}_b$ (0.1 K), which is highly significant for 25 samples ($p << 0.01$). The range of temperatures sampled at each transect-borehole intersection (up to 16 K) is poorly correlated ($r = -0.16$) with the $\overline{T}'_a$–$\overline{T}_b$ difference (up to 4.5 K). This relationship indicates that, at least for englacial temperatures between approximately −30 °C and −20 °C, a geometric mean (equation (8)) is acceptable when inferring $\overline{T}'_a$ from radar data using σ_∞ models that depend nonlinearly on temperature.

$\overline{T}'_a$ is typically less than −30 °C in the interior of the ice sheet, but it approaches −15 °C toward the ice-sheet margin (Figure 7a). $\widetilde{T}'_a$ is typically ~4 K, although in the southern portion of the ice sheet it is sometimes less than 3 K (Figure 7b). These relatively large uncertainties are related to the nonlinearity of $\overline{N}_a$ with temperature, such that relatively low $\overline{N}_a$ values lead to greater uncertainty in $\overline{T}'_a$. At cross-overs, the differences between values of $\overline{T}'_a$ are also normally distributed (Figure 5), with a best-fit cross-over difference of -0.3 ± 2.8 K, a distribution similar to that for $\overline{N}_a$.

We compare $\overline{T}'_a$ to both T_s and the depth-averaged (between z_{min} and z_{max}) modeled ice temperature $\overline{T}_m$ as differences of the form $\Delta T_s = \overline{T}'_a - T_s$ and $\Delta T_m = \overline{T}'_a - \overline{T}_m$, respectively (Figures 8 and 9). In southern Greenland, both surface and modeled temperatures are significantly higher than those inferred from radar. Across western Greenland, surface temperatures are consistently higher. Radar-inferred temperature generally agrees better with the depth-averaged modeled temperature ($r = 0.56$) than with surface temperature, as evidenced by the narrower distribution of differences between these values (Figure 9). However, in central northern Greenland, modeled temperatures are generally in worse agreement than with the surface temperature.

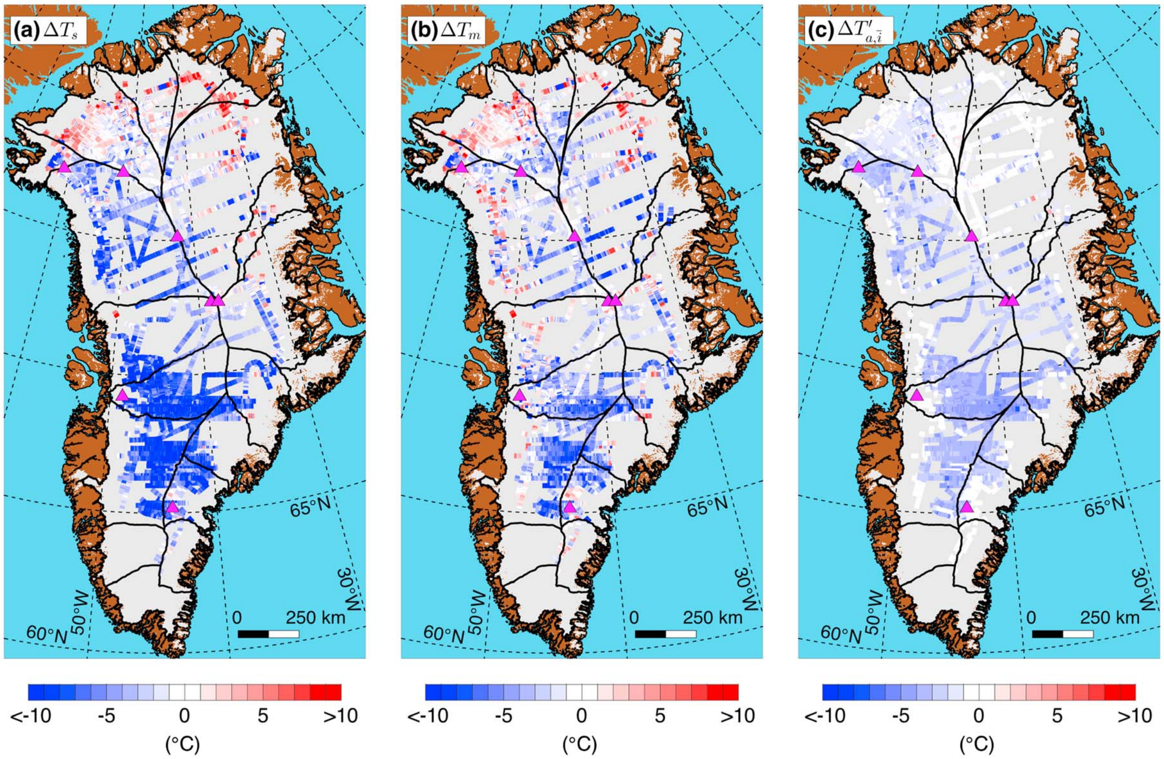

Figure 8. Difference between radar-inferred depth-averaged temperature and (a) mean annual surface temperature, $\Delta T_s = \overline{T}'_a - T_s$, (b) modeled depth-averaged ice temperature within the same depth interval, $\Delta T_m = \overline{T}'_a - \overline{T}_m$, and (c) radar-inferred depth-averaged temperature assuming uniform impurity concentrations (mean values at GRIP), $\Delta T_i = \overline{T}'_a - \overline{T}'_{a,\bar{i}}$. Negative (positive) differences are represented as blue (red) colors and indicate, e.g., $\overline{T}'_a < T_s$ ($\overline{T}'_a > T_s$).

We evaluate the importance of accounting for the spatial variation of chemistry by assuming that the relevant impurity concentrations are uniform throughout the GrIS and equal to their mean values at GRIP (0.8, 1.0, and 0.4 μM for [H^+], [Cl^-], and [NH_4^+], respectively). Figure 8c shows the difference $\Delta T_{a,\bar{i}} = \overline{T}'_a - \overline{T}'_{a,\bar{i}}$, where $\overline{T}'_{a,\bar{i}}$ is the radar-inferred depth-averaged temperature assuming uniform impurity concentrations. This difference is generally smaller than ΔT_s or ΔT_m, although it is rarely negligible, particularly in the western and southern GrIS. [H^+] is the dominant impurity in terms of its contribution to the radar attenuation [*MacGregor et al.*, 2007;

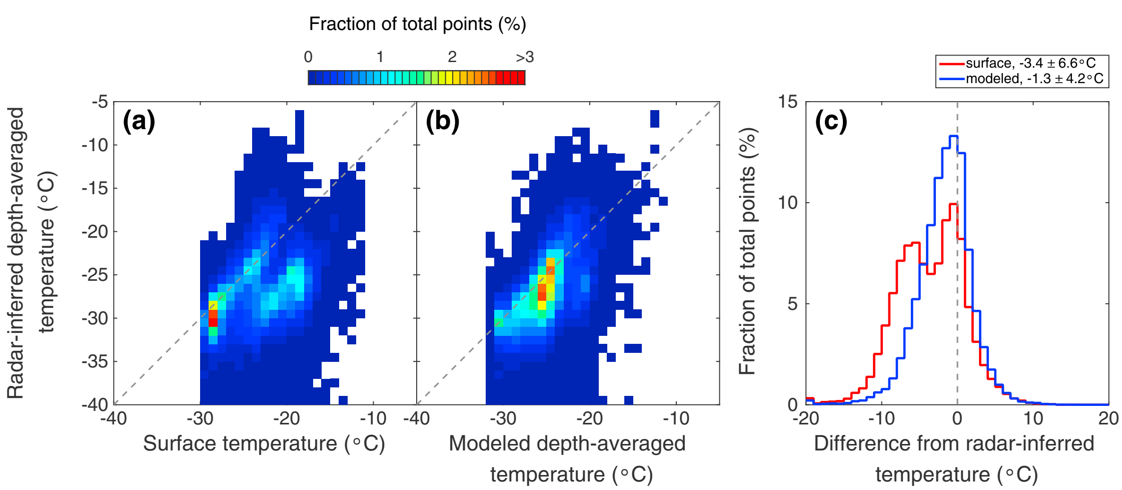

Figure 9. (a, b) Relationships between T_s, $\overline{T}_m$, and $\overline{T}'_a$. (c) Distribution of values of ΔT_s (red) and ΔT_m (blue). Legend gives best-fit mean and standard deviation for a Gaussian distribution.

Matsuoka et al., 2012] (Table 2). Its column-averaged value (0.8 μM) is one third lower than its mean value during the Holocene (1.2 μM), implying that an ice column composed primarily of Holocene ice will attenuate more than an ice column that also contains a significant proportion of LGP ice, assuming equivalent temperatures (Figure 3). The proportion of Holocene ice is greater in the western and southern GrIS, partly due to higher accumulation rates there [*MacGregor et al.,* 2015]. Where this age structure is not accounted for, impurity concentrations within the ice column will tend to be underestimated, leading to higher values of $T'_{a,\bar{i}}$ to explain a given estimate of $\overline{N}_a$ (Figure 3), consistent with the pattern of $\Delta T_{a,\bar{i}}$ (Figure 8c). Overall, the smaller values of $\Delta T_{a,\bar{i}}$ relative to $\overline{T}'_a$, and the relatively simple pattern of $\Delta T_{a,\bar{i}}$ suggests that most of the spatial variation of $\overline{N}_a$ is indeed due to spatially varying englacial temperature.

5. Discussion

5.1. Thermal State of the Greenland Ice Sheet

We now consider the contribution of these radar-inferred temperatures toward our understanding of the thermal state of the Greenland Ice Sheet. We first note that within 30 km of the *Lüthi et al.* [2002] boreholes, $\overline{T}'_a$ between 30 and 85% of the ice thickness is -23 ± 3 °C, which is similar to those borehole observations for the same relative depth range ($\overline{T}_b = -19.4$ to -21.1 °C; Figures 6e and 6f). The compatibility of these observations indicates that our approach can be used to interpret englacial temperature variability far from an ice divide, where nearly all the interior boreholes are located. However, given the large formal uncertainties associated with $\overline{T}'_a$ (Figure 7b) and the underlying assumptions used to generate them, we choose not to directly interpret absolute $\overline{T}'_a$ values in terms of the consequences of these temperatures for ice flow across the GrIS. Rather, we consider only the large-scale (>100 km) $\overline{T}'_a$ pattern and key features of its differences with surface and modeled temperatures (Figures 9a and 9b).

The primary $\overline{T}'_a$ pattern is of a cold interior surrounded by a warmer periphery. Given what is directly known of the thermodynamics of ice sheets [*Cuffey and Paterson*, 2010] and inferred for the GrIS in particular [e.g., *Rogozhina et al.,* 2011; *Aschwanden et al.,* 2012; *Seroussi et al.,* 2013], this pattern is unsurprising but likely influenced by several competing processes. We did not sample the entire ice column, and the sampled portion of the column tends to narrow toward the periphery of the ice sheet (Figures 4 and 6). Variability in the sampled portion of the ice column, particularly z_{min}, also affects interpretation of the $\overline{T}'_a$ pattern. A possible example of this sampling bias is the $\overline{T}'_a$ contrast across part of the central ice divide in the southern Greenland, which suggests colder ice immediately west of the ice divide, yet accumulation rates are higher east of this ice divide [*Ettema et al.,* 2009]. Setting aside these challenges in interpretation of smaller-scale (<100 km) changes in $\overline{T}'_a$, the ice-sheet wide pattern of $\overline{T}'_a$ emphasizes the importance of long-term surface boundary conditions (temperature and accumulation rate) in modulating the thermal state of a large portion of the GrIS, a conclusion similar to that of multiple modeling studies [*Huybrechts*, 1994; *Rogozhina et al.,* 2011; *Petrunin et al.,* 2013].

In southern and western Greenland, the dominant pattern for ΔT_s is of significantly colder ice at depth as compared to the surface ($\Delta T_s < 0$). To a lesser extent, ΔT_m displays a similar pattern, i.e., overestimated model temperature ($\Delta T_m < 0$). These patterns suggest that the "cold plug" at midrange depths observed in boreholes near the ice-sheet margin is present over a much larger area than is commonly inferred from models, even up to the central ice divide [*Funk et al.,* 1994; *Lüthi et al.,* 2002, 2015; *Brinkerhoff et al.,* 2011; *Harrington et al.,* 2005]. *Peters et al.* [2012] also inferred the presence of a cold plug of a similar magnitude to *Lüthi et al.* [2002] 50 km upstream of their boreholes, where we also estimate $\Delta T_s \approx -10$ K.

Closer to the ice-sheet margin, the cold plug is generally attributed to horizontal advection of ice from the colder ice-sheet interior [*Cuffey and Paterson*, 2010]. Horizontal advection is included in the ice-sheet model considered here, but the ΔT_m pattern suggests that the cold plug is not fully reproduced. Assuming that the model's thermodynamics accurately represent a steady state GrIS, this discrepancy is likely due to deviations of the modern GrIS from thermal steady state, i.e., changing past surface boundary conditions [*Rogozhina et al.,* 2012]. LGP and Holocene temperature and accumulation rate are known to have varied across the GrIS and particularly in southern Greenland [*Meese et al.,* 1994; *Cuffey et al.,* 1995; *Dahl-Jensen et al.,* 1998]. Temperature fluctuations were greater in southern Greenland, and accumulation rates were higher along the central ice divide. The combination of these spatiotemporal patterns likely acted to decrease ΔT_s, although additional modeling is needed to disentangle the key forcings. Because the ice we sampled in southern Greenland is mostly Holocene-aged [*MacGregor et al.,* 2015] and hence unlikely to have been significantly colder than the present surface higher past accumulation rates are likely the dominant control on the pattern of ΔT_s there.

A lower geothermal flux than expected could also contribute to the ΔT_m pattern in southern Greenland, but for the steady state model used, the geothermal flux was already assumed to be very low there ($<$40 mW m^{-2}). Alternatively, a much higher than expected geothermal flux ($>$ ~100 mW m^{-2}) could lead to rapid basal melting and an overall colder ice column. However, such a pattern would presumably be related to a degree of heterogeneity in southern Greenland's subglacial geology comparable to that believed to generate the Northeast Greenland Ice Stream, but without a comparable ice-flow feature. A higher geothermal flux could not lead directly to $\Delta T_s < 0$, and the basal melt rate would have to be greater than the local accumulation rate, which is high in this region ($>$35 cm a^{-1}), so such a pattern is unlikely to be sustained across such a large portion of the GrIS.

A pattern analogous to negative ΔT_m in southern Greenland has been identified in at least one other thermomechanical model of the GrIS. *Rogozhina et al.* [2011] simulated the late Pleistocene and Holocene history of the GrIS using both transient and steady state models. They found that steady state models forced using modern boundary conditions tended to overestimate the temperature structure as compared to transient models. Our observations and those modeling efforts indicate that steady state models are skewed warm in southern Greenland, although this skewness has limited effect on near-term predictions of sea-level rise due to GrIS mass loss [*Seroussi et al.,* 2013]. We thus consider it unlikely that these ΔT_s and ΔT_m patterns are due to a yet lower geothermal flux and consider past changes in surface boundary conditions the more likely explanation, a conclusion similar to that of *Rogozhina et al.* [2012]. Further, the apparent importance of horizontal heat advection within the southern GrIS emphasizes the general inadequacy of one-dimensional temperature models in representing its temperature structure there.

A similar pattern of colder ice is observed in central Greenland, although less consistently, partly due to coarser spatial coverage there. In northwestern Greenland and toward the northern periphery of the GrIS, both ΔT_s and ΔT_m are positive and their patterns are well correlated. There, the steady state model predicts a frozen bed and that this thermal state contiguously reaches the central ice divide [*Seroussi et al.,* 2013]. At a minimum, the pattern of ΔT_m suggests that the model underestimates englacial temperature in the northwest. Accumulation rates are higher there now than during the Holocene, as inferred from reflection geometry [*MacGregor et al.,* 2015]. An accumulation-rate change or a higher geothermal flux than expected (but not so high as to cause significant basal melting) could also explain this pattern.

From some of the same KU radar data used in this study, *Bell et al.* [2014] inferred that the GrIS has warmed in regions where significant basal freeze-on has occurred, most prominently in the onset region of Petermann Glacier in northwestern Greenland. Because very few reflections were traced within the basal units that likely contain frozen-on ice, we cannot directly evaluate warming within these units. A $>$5 K increase in $\overline{T}'_a$ is observed near Petermann Glacier's basal units, but it is based on reflections above these units, where we expect reduced warming from latent heat release. This pattern is also difficult to distinguish from the primary $\overline{T}'_a$ pattern of warming toward the ice-sheet periphery.

5.2. Implications of the Apparent Frequency Dependence of Radar Attenuation

The significant and consistent discrepancy between radar-inferred ($\overline{T}_a$) and borehole-measured ($\overline{T}_b$) englacial temperature suggests that a revision to existing σ_∞ models is required. Using ice-core and radar data, we present evidence that the frequency dependence of σ is nonnegligible between MF and VHF (Appendix C) and that this frequency dependence justifies a reasonable correction to the W97 σ_∞ model to reconcile $\overline{T}_a$ and $\overline{T}_b$. While we detected a small frequency dependence directly from the radar data, it was not significant. Accurate measurement of σ is notoriously difficult for low-loss materials between MF and VHF. Very few laboratory measurements span the relevant frequency range [*Matsuoka et al.,* 1996] and none exist for naturally formed ice. The closest suitable laboratory measurements for meteoric polar ice are those of *Stillman et al.* [2013a] between 10 mHz and 1 MHz, on which we base our inference. More dielectric measurements of ice cores across wide frequency ranges are needed to further clarify the effective frequency dependence of σ in ice sheets. Only a handful of studies have reported the change in echo intensity across a sufficiently large bandwidth to infer a frequency dependence in the total signal loss. Phase-sensitive radar also operates across a large bandwidth and may provide additional suitable data with which to evaluate this hypothesis [e.g., *Corr et al.,* 2002].

MacGregor et al. [2007] reported good agreement between the M07 σ_∞ model and the estimated radar-attenuation rate at Siple Dome, although we note that the radar-inferred value was slightly higher (~5%) than modeled. This agreement may be due to the lower frequency of the radar system employed (3–5 MHz) and the large range of frequencies and ice types used to determine the dielectric properties synthesized in the M07 model, which could obscure the effect of non-Debye dispersion (nonzero $\overline{\alpha}$). These relationships suggest that low-HF ground-based ice-penetrating radars and the inferences made from them in conjunction with existing σ_∞ models are less sensitive to frequency-dependent σ [e.g., *Jacobel et al.,* 2009, 2010].

The apparent frequency dependence of σ in the HF and VHF range for meteoric polar ice has implications for the interpretation of earlier multi-frequency radar studies of ice sheets and for the design of future ice-penetrating radar systems. Multifrequency radar systems have been used to study the nature of internal reflections [e.g., *Fujita et al.,* 1999; *Matsuoka et al.,* 2003]. These studies assumed that σ was frequency-independent, which enabled the evaluation of the frequency dependence of echo intensities as due to either conductivity (frequency-dependent) or permittivity (frequency-independent) contrasts and their further interpretation in terms of ice-sheet fabric. Assuming that the apparent value of $\overline{\alpha}$ for the GrIS (0.15) is also appropriate for the Antarctic ice sheet (Appendix C), the difference in $\overline{N}_a$ induced by the frequency difference of the systems used in those studies (60 and 179 MHz) is equivalent to $\beta \approx 1.2$. A β value of this magnitude is unlikely to significantly affect the interpretation of echo intensities in those studies, but it increases the uncertainty in their interpretations and that uncertainty also increases with depth. The importance of this putative effect is greater for our study because we interpreted spatial variation in $\overline{N}_a$ directly and in terms of another physical quantity (temperature), which required a σ_∞ model established using DEP data collected at a frequency much lower than that of the KU radar systems.

To evaluate the recent mass balance of the Greenland and Antarctic ice sheets, knowledge of the spatiotemporal variability of accumulation rates over the past millennium is valuable. This need has led to increasing interest in the shallow radiostratigraphy of ice sheets, which is best resolved using broadband VHF and ultrahigh frequency (UHF) radars [e.g., *Medley et al.,* 2013; *Rodríguez-Morales et al.,* 2014]. The designs of such radar systems should account for increasing dielectric attenuation with increasing frequency. Echo intensities from such systems are beginning to be investigated [e.g., *Lewis et al.,* 2015] and such studies should be sensitive to the frequency dependence of σ. At UHF, the low-frequency tail of the infrared resonance of ice is also a concern [*Moore and Fujita*, 1993].

Nonnegligible power loss due to volume scattering (L_{vs}) and/or birefringence (L_b) could also contribute to the discrepancy between $\overline{T}_a$ and $\overline{T}_b$. Because $\beta \approx 2.6$, the integrated two-way power loss due to L_{vs} and L_b would have to be greater than $(L_a)^2$ to explain our observations; e.g., $(L_{vs} + L_b)$ would have to be ~ -30 dB through a 3.8 km long roundtrip at NEEM to reconcile $\overline{T}_a$ and $\overline{T}_b$ using the uncorrected W97 σ_∞ model. Although L_{vs} and L_b are difficult to constrain independently, these phenomena are considered unlikely to produce such losses in the interiors of polar ice sheets at or near ice divides, where most of the boreholes are located. $(L_{vs} + L_b)$ would also have to be temperature-dependent in a manner similar to that predicted for $\overline{N}_a$, which we consider unlikely.

Another possible confounding factor regarding our interpretation of the $\overline{T}_a$–$\overline{T}_b$ discrepancy is the assumption of specularity of the internal reflections. The correction for geometric spreading (equation (2)) relies critically on the nature of the reflector and its radar cross-section. For the bed reflector, the specularity assumption is not likely to be acceptable across a whole ice sheet [e.g., *Schroeder et al.,* 2013], but the specularity of most internal reflections is commonly assumed and exploited. A preliminary investigation of the sensitivity of P_r to the width of the SAR focusing beamwidth suggests that as this beamwidth increases (decreasing along-track resolution), the echo intensity of some deeper internal reflections ($z > 1500$ m) can increase by several decibels. This relationship suggests that some deeper reflections are not perfectly specular.

If an internal reflection is not perfectly specular, then the exponent associated with the geometric spreading correction is greater than 2, leading to lower radar-inferred attenuation rates and temperatures and hence a lower apparent frequency dependence for σ. If we assume that geometric spreading exponent is 3, equivalent to assuming that the internal reflections are due to rough, planar reflectors [e.g., *Davis and Annan*, 1989], then GrIS-wide $\overline{N}_a$ values decrease by less than 10% and $\overline{T}_a$ by ~1 K. This situation occurs because we normalize P_r with respect to the value of the shallowest reflection (equation (3)) and because the pattern of geometric spreading loss with increasing depth does not change significantly. Relaxing the specularity assumption for all reflections therefore cannot explain the $\overline{T}_a - \overline{T}_b$ discrepancy, so we report only $\overline{N}_a$ values based on the assumption of perfect specularity.

The primary set of potential confounding factors in our interpretation of $\overline{N}_a$ in terms of englacial temperature (nonuniform R, nonnegligible L_{vs} or L_b or nonspecular reflections) suggests that our estimate of β for model W97 will be biased toward overestimating the true frequency dependence of $\overline{N}_a$. However, the combination of the above evaluation and the ice-core analysis (Appendix C) strongly suggests that this set of potential confounding factors is insufficient as an alternative explanation for the apparent frequency dependence of $\overline{N}_a$. Poorly constrained uncertainty in some of the dielectric properties that form the σ_∞ models (Table 2) suggests that our direct application of these models may also affect interpretation of $\overline{N}_a$, but the potential bias associated with those uncertainties is unclear.

6. Conclusions

Following an existing method, we estimated depth-averaged radar-attenuation rates throughout a substantial fraction of the GrIS using an extensive ice-penetrating radar data set and its associated radiostratigraphy. Radar-attenuation rates generally increase toward the periphery of the ice sheet. By accounting for spatially varying chemistry and comparing radar-inferred englacial temperature with that measured in boreholes, we corrected the radar-inferred temperatures and mapped their spatial variation across the GrIS. The comparison with boreholes also confirms unambiguously that englacial radar attenuation is temperature-dependent and that this temperature dependence is well represented by existing models. Differences between radar-inferred temperature and an existing steady state model are likely due to past surface boundary conditions that differ from modern values and are not accounted for by the model, although uncertainty in the geothermal flux and past rates of horizontal advection may also contribute to these differences. This result represents a novel evaluation of a temperature model for an ice sheet.

Based on this study alone, radar-inferred ice-sheet temperatures are not yet reliable enough to justify direct interpretation of their absolute values or their relative variation with depth, particularly given the simplifying assumptions of vertically uniform radar reflectivity and attenuation rate. We thus interpret primarily the horizontal spatial variation in the pattern of radar-inferred depth-averaged temperature. The correspondence between radar-inferred and borehole-measured temperatures demonstrates that additional information regarding ice temperature can be recovered from radar. Such information is unlikely to replace borehole thermometry, but it could provide a vertically coarse but horizontally extensive constraint on temperature, similar to the relationship between ice-core depth-age scales and radar-mapped isochrones. Such information could potentially be assimilated into ice-sheet models to improve confidence in them, as is now done with satellite-altimetry data [*Larour et al.*, 2014].

Our results further emphasize the conclusions of *Holschuh et al.* [2014], in that radar surveys of large ice masses ought to consider system and survey designs that optimize recovery of both the geometry and echo intensity of internal reflections, so that maximum recovery of geophysical information is possible. Because the data we used were not collected with the present study in mind, our results also demonstrate that past radar surveys of large ice masses that detected extensive radiostratigraphy may have further value in terms of constraining englacial temperature. Such surveys include the earlier GrIS KU data for which reflections were traced by *MacGregor et al.* [2015], but whose echo intensities cannot be reliably interpreted presently. Borehole-temperature profiles are critical for understanding ice-sheet temperature history and rheology, and our results demonstrate that more of these profiles should be collected away from ice divides, where horizontal advection and past climate forcings can have a greater impact on the local temperature structure.

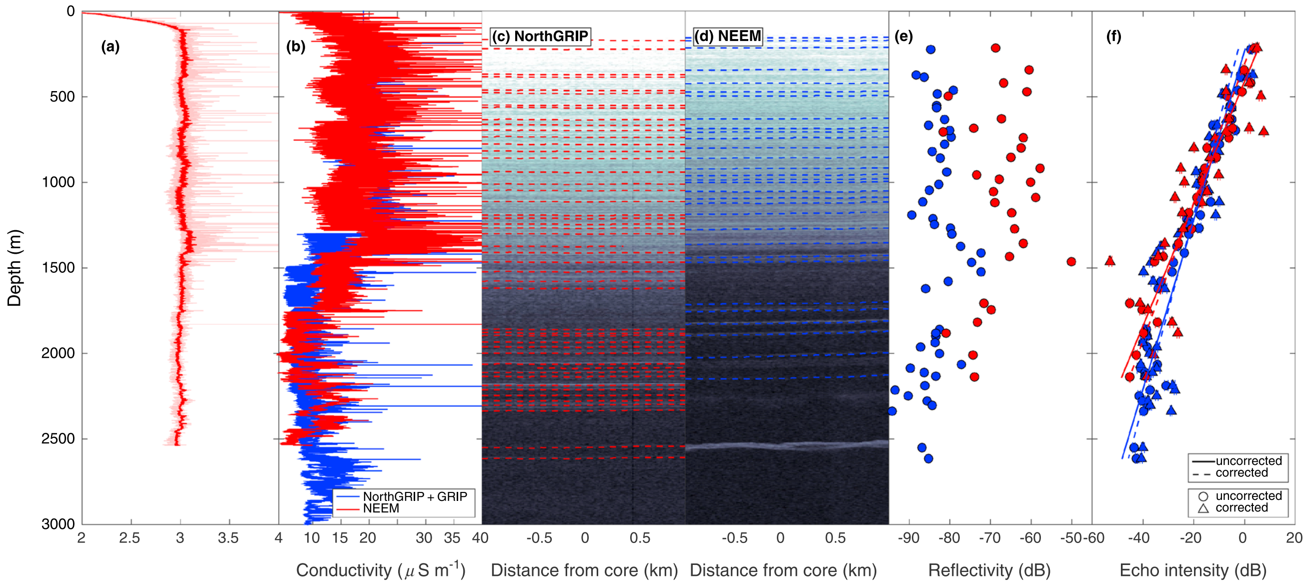

Figure A1. (a, b) DEP-measured permittivity (ε') and conductivity (σ_∞), respectively, for the NorthGRIP (blue) and NEEM (red) ice cores [*Rasmussen et al.*, 2013]. Note that these data have not been temperature corrected, and conductivity profile for NorthGRIP is spliced with that of GRIP. (c, d) Radargram from 6 May 2011 (same as Figure 2) in the vicinity of the NorthGRIP and NEEM ice cores, respectively. Distance is relative to point of closest core intersection. (e) Modeled Fresnel reflectivity matched to traced reflections. (f) Uncorrected and reflectivity corrected [P_{rc}], and best-fit depth-loss relationships.

Finally, this study suggests multiple avenues of research on the relationship between radar attenuation and temperature. Such studies ought to include direct investigations of the frequency dependence of the electrical conductivity of meteoric polar ice at radar frequencies, localized in situ measurements of englacial dielectric attenuation [e.g., *Winebrenner et al.*, 2003], evaluation of the specularity of internal reflections, and improvements to the sensitivity of deep-sounding ice-penetrating radars. Such research could help address the primary limitation of this study—the recovery of a depth-averaged temperature only—so that subsequent analyses may potentially resolve vertical temperature gradients.

Appendix A: Assumption of Uniform Radar Reflectivity

To evaluate our assumption of uniform reflectivity R for estimating $\overline{N}_a$, we examine the available portions of the GRIP, NorthGRIP, and NEEM DEP profiles (Figures A1a and A1b). We calculate the Fresnel reflectivity following *Paren* [1981] where the permittivity (conductivity) contrast exceeds a threshold value of 0.001 (2 μS m^{-1}). For NorthGRIP, only the incomplete DEP conductivity profile is available, so we include portions of the GRIP DEP conductivity profile and ignore the contribution from permittivity contrasts. For NEEM, both the permittivity and conductivity profiles are available. None of these DEP profiles are temperature corrected.

The mean reflectivity $[\overline{R}]$ of these contrasts is -83.6 ± 4.6 dB for NorthGRIP and -77.6 ± 7.4 dB for NEEM (Figure A1e). The transect shown in Figure 2 intersected both the NorthGRIP and NEEM ice cores (Figures A1c and A1d). We match its core-intersecting reflections with the DEP-inferred reflectivities [R_i] and use these reflectivities to adjust $[P^i_{rc}]$ as $[P^i_{rc}] - ([R_i] - [\overline{R}])$ and recalculate $\overline{N}_a$. The uncorrected attenuation rates at NorthGRIP and NEEM estimated from the 6 May 2011 transect are 10.1 ± 0.5 and 14.1 ± 0.6 dB km^{-1}, respectively. Once corrected for the DEP-inferred reflectivity, these attenuation rates are 9.0 ± 0.7 and 12.4 ± 1.7 dB km^{-1}, respectively. These corrected values are more uncertain due to the large range of [R_i]. These results show that nonuniform R can certainly affect estimation of $\overline{N}_a$ and in some cases significantly.

Because the available DEP profiles are incomplete and not temperature corrected, these estimates of englacial reflectivity should be considered simple approximations and likely underestimates. A more complete analysis of DEP data could improve reflectivity estimates, e.g., by numerical electromagnetic modeling [*Eisen et al.*, 2003]. However, such estimates would still be limited by the sparse distribution of ice cores and require the assumption that R_i is horizontally uniform. Hence, we consider the assumption of uniform R acceptable for this study.

Appendix B: HF-Limit Conductivity Models

For model M07, *MacGregor et al.* [2007] synthesized these properties (except for NH_4^+) for both naturally formed and laboratory-frozen ice and reported good agreement between modeled and HF-radar-inferred attenuation rates at Siple Dome in West Antarctica, depending on the values of the dielectric properties used. The most poorly constrained of these dielectric properties are those of pure ice. Here we use the dielectric properties of pure ice from the adjusted model of *MacGregor et al.* [2007]. The σ_∞ model described by *MacGregor et al.* [2007] has not been applied previously to the study of radar attenuation within the GrIS, where $[NH_4^+]$ is typically higher than for the Antarctic ice sheet [*Legrand and Mayewski*, 1997]. Hence, for model M07, we use the value of $\mu_{NH_4^+}$ reported by *Wolff et al.* [1997] and the same value of $E_{NH_4^+}$ as for the second σ_∞ model (W97).

The second σ_∞ model (W97) is based on that given by *Wolff et al.* [1997] and additional insights into the physical underpinnings of this model provided by *Stillman et al.* [2013a, 2013b]. Those studies clarified that the dominant HF-limit conduction mechanism in meteoric polar ice is the movement of charged protonic point defects (following Jaccard theory) and that the conductivity contribution of NH_4^+ is instead mostly due to enhanced lattice portioning of Cl^-. These discoveries can explain—but not immediately resolve—the large reported range of some of ice's dielectric properties, particularly for laboratory-frozen ice. In particular, impurity partitioning between the ice lattice and grain boundaries is a key unknown associated with the synthesis of ice's HF dielectric properties reported by *MacGregor et al.* [2007]. This situation motivates consideration of a second σ_∞ model. Based on DEP measurements of the GRIP ice core, an empirical relationship for σ_∞ at $-15\,°C$ and 300 kHz is [*Wolff et al.,* 1997]

$$\sigma_\infty = 9 + 4\,[H^+] + 1\,[NH_4{}^+] + 0.55\,[Cl^-], \tag{B1}$$

where the units of σ_∞ are $\mu S\,m^{-1}$ and the molarity units are μM ($\mu mol\,L^{-1}$). The DEP-inferred value of σ_{pure} ($9\ \mu S\,m^{-1}$) agrees well with other laboratory measurements [*Stillman et al.,* 2013a]. In equation (B1), the coefficients associated with impurities are effective molar conductivities appropriate for the GRIP ice core, and we assume that they are also valid for the GrIS as a whole. These effective molar conductivities account indirectly for the partitioning of these impurities between the ice lattice, where they can increase σ_∞ by creating extrinsic protonic point defects, and grain boundaries, where these impurities may also reside but do not typically affect σ_∞ in meteoric polar ice [*Stillman et al.,* 2013a].

Equation (B1) does not account for the codependence of the NH_4^+ and Cl^- contributions to σ_∞ [*Stillman et al.,* 2013b] nor does it specify a temperature dependence for the different contributions to σ_∞. For the activation energy of the conductivity of pure ice E_{pure}, we use 0.58 eV, based on analysis of measurements by *Kawada* [1978], as their ice samples have been shown indirectly to be the purest laboratory-made ice yet measured electrically [*Stillman et al.,* 2013a]. For the activation energy of the conductivity contribution from impurities, we use 0.21 eV for ionic defects (H^+) and 0.23 eV for Bjerrum defects (Cl^- and NH_4^+), which are suitable activation energies for the mobilities of these extrinsic lattice defects [*Stillman et al.,* 2013a].

Appendix C: Frequency Dependence of HF-Limit Conductivity

For meteoric polar ice, σ is commonly assumed to be frequency-independent between the lower end of the MF range and the upper end of the VHF range [e.g., *Moore and Fujita*, 1993; *Matsuoka et al.,* 1996, 2003; *Fujita et al.,* 1999, 2000; *MacGregor et al.,* 2007]. This assumption of frequency independence is based on a classical interpretation of the electrical loss mechanism as due to a Debye relaxation of protonic point defects in the ice lattice in the presence of an alternating electric field. Broadband (10 mHz to 1 MHz) measurements of the dielectric properties of ice by *Stillman et al.* [2013a, 2013b] confirm that such relaxations are the dominant loss mechanism in meteoric polar ice. However, these relaxations do not always clearly follow the Debye model, an observation that has important consequences for the frequency dependence of σ. Separately, several other studies have observed a slight frequency dependence in signal loss across the VHF and

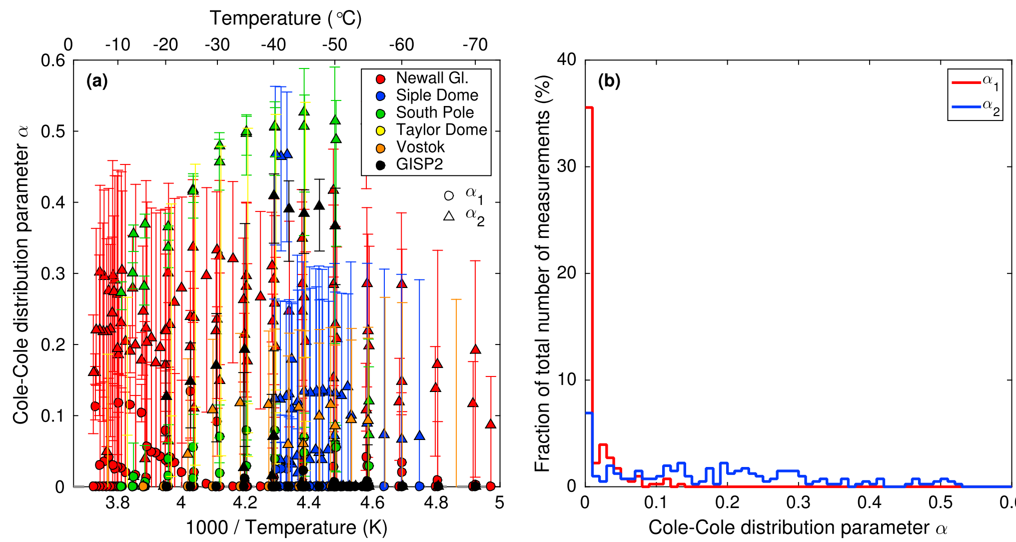

Figure C1. (a) Temperature dependence of α for the fastest two relaxations (two lowest values of τ) in the Greenland and Antarctic ice cores studied by *Stillman et al.* [2013a]. Circles represent the fastest relaxation ($j = 1$ in equation (C1)) and triangles represent the second fastest ($j = 2$). Error bars represent the 95% confidence intervals for each value where available. (b) Distribution of inferred values of α_1 and α_2.

ultrahigh frequency (UHF) ranges in Greenland and Antarctica. Here we consider the significance of these findings for the purposes of correcting our σ_∞ models and correcting $\overline{T}_a$ within the GrIS using VHF radar data.

The complex permittivity of ice ε^* can be expressed in Cole-Cole form as [e.g., *Stillman et al.,* 2013a]

$$\varepsilon^* = \varepsilon' - i\varepsilon'' = \varepsilon_\infty + \left[\sum_{j=1}^{m} \frac{\Delta\varepsilon_j'}{1 + (i\omega\tau_j)^{1-\alpha_j}}\right] - \frac{i\sigma_{\mathrm{DC}}}{\varepsilon_0\omega}, \tag{C1}$$

where ε' and ε'' are the real and imaginary parts of ε^*, respectively, ε_∞ is the HF-limit permittivity, m is the total number of observed dielectric relaxations, $\Delta\varepsilon'$ is the dielectric susceptibility, τ is the temperature- and impurity-dependent relaxation time, α is the Cole-Cole distribution parameter, $i = \sqrt{-1}$, σ_{DC} is the direct-current (DC) conductivity, and ω is the angular frequency. *Stillman et al.* [2013a] showed that for meteoric polar ice, the DC contribution to ε'' (last term in equation (C1)) is negligible at frequencies two or more decades above the relaxation frequency $f_r = 1/2\pi\tau$ (~10^2–10^3 Hz) and, critically, that multiple relaxations are present in meteoric ice ($m > 1$).

A Debye relaxation is one for which $\alpha = 0$. A nonzero value of α indicates a lognormal distribution of relaxation times, with a proportion of those relaxations associated with lower (higher) values of τ (f_r) [*Cole and Cole*, 1941]. Figure C1 shows the values of α inferred from *Stillman et al.*'s [2013a] measurements of 26 samples from six deep Greenland and Antarctic ice cores. Although poorly constrained, α is often greater than zero and not clearly temperature dependent, including for samples from the GISP2 ice core from the central GrIS. For the fastest ($j = 1$) relaxation and second-fastest ($j = 2$) relaxations (i.e., lowest two τ values, equivalent to the two highest f_r values), the unweighted mean values of α are 0.01 ± 0.03 and 0.20 ± 0.14, respectively.

For these two fastest relaxations, their respective $\Delta\varepsilon'$ values are variable but comparable in magnitude. τ_1 is typically an order of magnitude smaller than τ_2, although this range narrows at higher temperatures (> -40 °C) more typical of the GrIS [*Stillman et al.,* 2013a]. Following equation (C1), these relationships indicate that the bulk value of α (α_{bulk}) for a given sample will tend toward α_1, rather than α_2, but that α_{bulk} is unlikely to be negligible for meteoric polar ice. The fastest observed relaxations are typically consistent with those of laboratory-frozen ice that is saturated in extrinsic defects [*Stillman et al.,* 2013a], so yet lower values of τ_1 are unlikely and the near-zero distribution of α_1 is consistent with this interpretation (Figure C1b). Conversely, the second-fastest set of relaxations is closer to that of pure ice, so a greater range of defect concentrations (and hence τ_2 values) is possible, consistent with the higher and broader distribution of α_2.

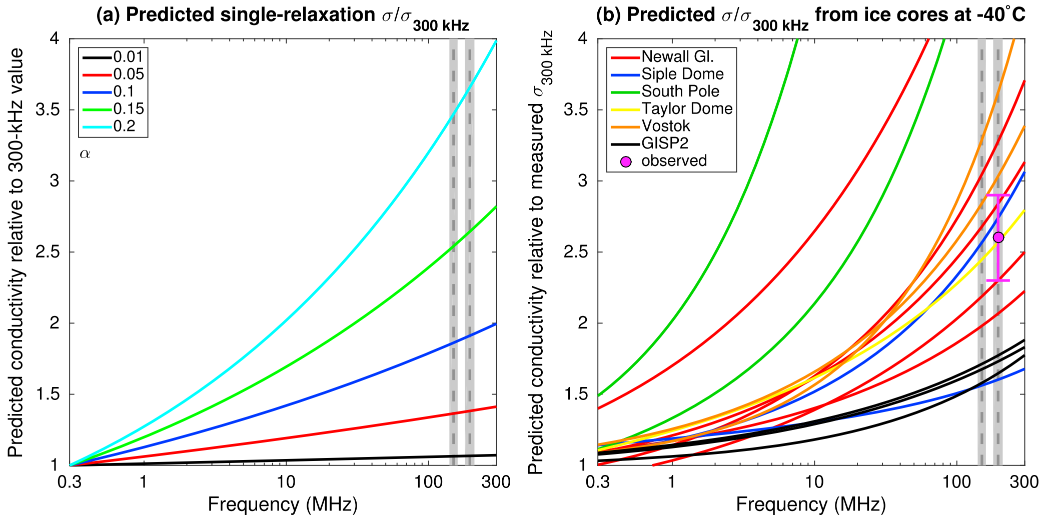

Figure C2. $\sigma/\sigma_{300\mathrm{kHz}}$ as a function of α (values in legend) and frequency, following equation (C4). Values are relative to the DEP HF-limit frequency (300 kHz). For this example, $\Delta\varepsilon' = 100$ and $\tau = 8 \times 10^{-4}$ s, which are typical values for meteoric polar ice [*Stillman et al.,* 2013a]. Vertical gray dashed lines and fill represent center frequencies and bandwidths, respectively, of the three radar systems whose data were used in this study (ACORDS, MCRDS: 140–160 MHz; MCoRDS: 180–210 MHz). (b) Predicted frequency dependence of $\sigma/\sigma_{300\mathrm{kHz}}$ at −40 °C (following equation (C1)) for the samples measured by *Stillman et al.* [2013a], whose α values are shown in Figure A1. Nonunity values at $f = 300$ kHz indicate a discrepancy between the measured value of σ between 10 and 100 kHz (assumed to be valid at 300 kHz) and that inferred from the best-fit parameters for (α, τ, $\Delta\varepsilon'$, and σ_{DC}) and equation (C1). The observed value of $\sigma/\sigma_{300\mathrm{kHz}}$, shown in magenta, is that which is necessary to reconcile $\overline{T}_a$ (model W97) and $\overline{T}_b$, i.e., $\overline{\beta}\ \pm\widetilde{\beta}$ Only McORDS transects intersected the interior boreholes used in this study.

By definition, σ is [e.g., *Moore and Fujita*, 1993]

$$\sigma = \omega\varepsilon_0\varepsilon''. \tag{C2}$$

Considering only one relaxation for simplicity, when $\alpha = 0$, equation (C2) becomes

$$\sigma = \frac{\omega^2\tau\varepsilon_0\Delta\varepsilon'}{1+\omega^2\tau^2}. \tag{C3}$$

ε_0 and $\Delta\varepsilon'$ are frequency-independent by definition, therefore equation (C3) is essentially frequency independent above the bulk relaxation frequency and becomes σ_∞. When $\alpha \neq 0$, equation (C2) becomes

$$\sigma = \omega\varepsilon_0 \mathrm{Im}\left[\frac{\Delta\varepsilon'}{1+(i\omega\tau)^{1-\alpha}}\right], \tag{C4}$$

which is frequency dependent ($\sigma \propto \omega^\alpha$). Figure C2 shows the effect of nonzero values of α on σ for a plausible range of α values, based on Figure C1. Figure C2 also shows the σ range inferred from fits to *Stillman et al.*'s [2013a] ice-core measurements using equation (C1). Note that the predicted frequency dependence of σ shown in Figure C2b is derived using data collected at −40 °C, the temperature at which the largest number of samples was measured. This temperature is somewhat below the expected range for the GrIS (e.g., Figure 6). At higher temperatures, the range of τ values for multiple relaxations narrows, due to differing activation energies [*Stillman et al.,* 2013a], suggesting that the frequency dependence of σ will increase (higher β) given the presence of at least one relaxation with a nonzero α value.

Paden et al. [2005] observed an 8 ± 2.5 dB increase in signal loss from the bed at NorthGRIP between 110 and 500 MHz. This frequency range includes the full bandwidth of the KU radar data considered in this study. *Matsuoka et al.* [2009] attributed periodic deviations from the linear trend in the frequency dependence of this signal loss to englacial birefringence. Assuming that this overall increase in signal loss (the linear trend in decibels) is attributable entirely to the frequency dependence of σ_∞, it is equivalent to an increase in $\overline{N}_a$ of 1.3 ± 0.4 dB km^{-1} or an increase in the depth-averaged value of σ_∞ of 1.4 ± 0.4 μS m^{-1}. At NorthGRIP, we estimate $\overline{N}_a$ = 10.1 ± 0.4 dB km^{-1} through 79% of the ice column, or σ_∞ = 11.0 ± 0.4 μS m^{-1}. Following equation (C4) and assuming that our estimate of $\overline{N}_a$ is equivalent to that for the full ice thickness, *Paden et al.*'s [2005] reported frequency dependence is equivalent to a depth-averaged α_{bulk} = 0.08 ± 0.02. This value is comparable to that of $\overline{\alpha}_2$ for the GISP2 samples measured in the laboratory by *Stillman et al.* [2013a] (Figure C1a; 0.08 ± 0.14). Given potential confounding factors for the frequency dependence reported by *Paden et al.* [2005] (e.g., frequency-dependent bed reflectivity) and our likely underestimate of $\overline{N}_a$ for the full ice thickness at NorthGRIP, this value may represent an upper limit on α_{bulk} at NorthGRIP. For Model W97 (equation (B1)), which is based on the GRIP DEP record, this frequency difference implies that $\sigma_{195\text{ MHz}}/\sigma_{300\text{ kHz}}$ = 1.7 between the DEP and MCoRDS operating frequencies, respectively. This value is also comparable to that inferred from Greenland ice-core samples (Figure C2b).

For the Antarctic ice sheet, *Barrella et al.* [2011] estimated radar attenuation within the Ross Ice Shelf between 75 and 1250 MHz. They inferred a ~67% increase in $\overline{N}_a$ across this frequency range that increase nearly linearly with increasing frequency, implying that $\overline{\alpha} \approx$ 0.18. At the same location, *Hanson et al.* [2015] inferred a 37% increase in $\overline{N}_a$ between 100 and 850 MHz, implying that $\overline{\alpha} \approx$ 0.15. For their particular study area, *Hanson et al.* [2015] presented evidence the ice-seawater interface was specular between 100 and 850 MHz, implying that the increase $\overline{N}_a$ is indeed due to the hypothesized englacial frequency dependence of radar attenuation and not the roughness-induced frequency dependence of the ice-seawater reflectivity.

Notation

P_r	radar received power (echo intensity).
R	reflectivity of internal reflections.
P_t	transmitted power.
λ_{air}	radar wavelength in air.
G_a	antenna gain.
T	transmission loss at air-ice interface.
L_a	one-way loss due to englacial dielectric attenuation.
L_{vs}	total loss due to englacial volume scattering.
L_b	total loss due to englacial birefringence.
L_{sys}	total system loss.
G_p	processing gain.
h	height of the aircraft above ice surface.
z	depth.
$\varepsilon'_{\text{ice}}$	real part of the complex relative permittivity of pure ice.
P_{rc}	geometrically- and slope-corrected echo intensity.
ΔP^i_{rc}	difference in echo intensity between the first and *i*th observed reflections.
ΔL^i_a	total attenuation within the ice column between the first and *i*th observed reflections.
$\overline{N}_a$	depth-averaged radar-attenuation rate.
Δz	depth difference between two vertically consecutive observed reflections.
b	zero-intercept in (5).
$\tilde{N}_a$	uncertainty in depth-averaged radar-attenuation rate.
$\tilde{P}^i_{rc}$	standard deviation of echo intensity of *i* th reflection within 1-km segment.
h	portion of the ice column between the shallowest and deepest observed reflections.
H	ice thickness.
z_{min}	shallowest observed reflection.
z_{max}	deepest observed reflection.
σ_∞	HF-limit ice conductivity.
ε_0	permittivity of the vacuum.
c	speed of light in the vacuum.
σ	ice conductivity.

E_{pure}, E_{H^+}, E_{Cl^-}, $E_{NH_4^+}$,	activation energies of the conductivity contributions from pure ice, H^+, Cl^-, and NH_4^+, respectively.
μ_{H^+}, μ_{Cl^-}, $\mu_{NH_4^+}$	molar conductivities of H^+, Cl^-, and NH_4^+ impurities, respectively.
k	Boltzmann constant.
T	temperature.
T_r	reference temperature.
$\overline{T}_a$	radar-inferred, depth-averaged ice temperature.
n	number of observed reflections.
$\widetilde{T}_a$	uncertainty in radar-inferred ice temperature.
T_s	mean annual surface temperature.
$\overline{T}_b$	borehole-measured, depth-averaged ice temperature.
$\Delta\overline{T}_c$	best-fit temperature difference radar-inferred and borehole-measured ice temperature.
β	correction factor for the W97 σ_∞ model.
$\overline{T}_a^{'}, \widetilde{T}_a^{'}$	corrected, radar-inferred, depth-averaged ice temperature and its uncertainty, respectively.
$\overline{T}_m$	depth-averaged modeled ice temperature.
ΔT_s	difference between corrected depth-averaged radar-inferred and mean annual surface temperatures.
ΔT_m	difference between corrected radar-inferred and modeled depth-averaged ice temperatures.
$\overline{T}_{a,\bar{i}}^{'}$	corrected depth-averaged radar-inferred temperature assuming uniform impurity concentrations.
$\Delta T_{a,\bar{i}}^{'}$	difference between corrected depth-averaged radar-inferred temperatures, assuming spatially varying and uniform impurity concentrations, respectively.
R_i	DEP-inferred Fresnel reflectivity.
$\overline{R}$	mean DEP-inferred Fresnel reflectivity.
ε^*, ε', ε''	complex, real, and imaginary parts of permittivity, respectively.
ε_∞	HF-limit permittivity.
m	number of dielectric relaxations.
$\Delta\varepsilon'$	dielectric susceptibility.
ω	radial frequency.
τ	relaxation time.
α	Cole-Cole distribution parameter.
σ_{DC}	DC conductivity.
f_r	relaxation frequency.

Acknowledgments
NSF (ARC 1107753 and 1108058; ANT 0424589) and NASA (NNX12AB71G) supported this work. We thank the organizations (Program for Arctic Regional Climate Assessment, Center for Remote Sensing of Ice Sheets, and Operation IceBridge) and innumerable individuals that both supported and performed the collection and processing of the radar data used in this study. We thank S. Anandakrishnan, K. Matsuoka, and D.P. Winebrenner for the inspiration for this work; the Centre for Ice and Climate for the DEP data; and L.C. Andrews, K.A. Christianson, C. Grima, J.C. Hiester, N. Holschuh, K. Thirumalai, and D.A. Young for valuable discussions. We thank Associate Editor J.N. Bassis, D.M. Schroeder, and an anonymous referee for valuable comments that improved this manuscript. Echo-intensity data will be archived at the National Snow and Ice Data Center (NSIDC; http://www.nsidc.org).

References

Alley, R. B., R. G. Finke, K. Nishiizumi, S. Anandakrishnan, C. A. Shuman, G. Mershon, G. A. Zeilenski, and P. A. Mayewksi (1995), Changes in continental and sea-salt atmospheric loadings in central Greenland during the most recent deglaciation: Model-based estimates, *J. Glaciol.*, *41*(139), 503–514.

Alley, R. B., P. U. Clark, P. Huybrechts, and I. Joughin (2005), Ice-sheet and sea-level changes, *Science*, *310*, 456–460.

Aschwanden, A., E. Bueler, C. Khroulev, and H. Blatter (2012), An enthalpy formulation for glaciers and ice sheets, *J. Glaciol.*, *58*(209), 441–457, doi:10.3189/2012JoG11J088.

Barrella, T., S. Barwick, and D. Saltzberg (2011), Ross Ice Shelf (Antarctica) in situ radio-frequency attenuation, *J. Glaciol.*, *57*(201), 61–66.

Bell, R. E., et al. (2014), Warming and deformation of the Greenland Ice Sheet by refreezing meltwater, *Nat. Geosci.*, *7*, 497–502, doi:10.1038/ngeo2179.

Bogorodsky, V. V., C. R. Bentley, and P. Gudmandsen (1985), *Radioglaciology*, 1st ed., D. Reidel, Dordrecht, Holland.

Brinkerhoff, D. J., T. W. Meierbachtol, J. V. Johnson, and J. T. Harper (2011), Sensitivity of the frozen/melted basal boundary condition to perturbations of basal traction and geothermal heat flux: Isunnguata Sermia, western Greenland, *Ann. Glaciol.*, *52*(59), 43–50.

Carter, S. P., D. D. Blankenship, D. A. Young, and J. W. Holt (2009), Using radar data to identify the sources and distribution of subglacial water in radar-sounding data: Application to Dome C, East Antarctica, *J. Glaciol.*, *55*(194), 1025–1040.

Cole, K. S., and R. H. Cole (1941), Dispersion and absorption in dielectrics. I. Alternating current characteristics, *J. Chem. Phys.*, *9*, 341–351.

Christianson, K., et al. (2014), Dilatant till facilitates ice-stream flow in northeast Greenland, *Earth Planet. Sci. Lett.*, *401*, 57–69, doi:10.1016/j.epsl.2014.05.060.

Chuah, T. (1997), Design and development of coherent radar depth sounder for measurement of Greenland ice sheet thickness, PhD thesis, Univ. Kansas.

Clow, G. D. (2008), USGS polar temperature logging system, description and measurement uncertainties, USGS Tech. Meth., 2-E3, 24 pp.

Clow, G. D. (2014), Temperature data acquired from the DOI/GTN-P Deep Borehole Array on the Arctic Slope of Alaska, 1973–2013, *Earth Syst. Sci. Data*, *6*, 1–18, doi:10.5194/essd-6-201-2014.

Clow, G. D., R. W. Slatus, and E. D. Waddington (1996), A new high-precision borehole-temperature logging system used at GISP2, Greenland, and Taylor Dome, Antarctica, *J. Glaciol.*, *42*(142), 576–584.

Corr, H. F. J., J. C. Moore, and K. W. Nicholls (1993), Radar absorption due to impurities in Antarctic ice, *Geophys. Res. Lett.*, *20*(11), 1071–1074, doi:10.1029/93GL01395.

Corr, H. F. J., A. Jenkins, K. W. Nicholls, and C. S. M. Doake (2002), Precise measurement of changes in ice-shelf thickness by phase-sensitive radar to determine basal melt rates, *Geophys. Res. Lett.*, *29*(8), 1232, doi:10.1029/2001GL014618.

Corr, H. F. J., and D. G. Vaughan (2008), A recent volcanic eruption beneath the West Antarctic ice sheet, *Nat. Geosci.*, *1*(2), 122–125, doi:10.1038/ngeo106.

Cuffey, K. M., and G. D. Clow (1997), Temperature, accumulation, and ice sheet elevation in central Greenland through the last deglacial transition, *J. Geophys. Res.*, *102*(C12), 26,383–26,396, doi:10.1029/96JC03981.

Cuffey, K. M., and W. S. B. Paterson (2010), *The Physics of Glaciers*, 4th ed., 693 pp., Elsevier, Burlington, Mass.

Cuffey, K. M., G. D. Clow, R. B. Alley, M. Stuiver, E. D. Waddington, and R. W. Saltus (1995), Large Arctic temperature change at the Wisconsin-Holocene glacial transition, *Science*, *270*, 455–458.

Dahl-Jensen, D., K. Mosegaard, N. Gundestrup, G. D. Clow, S. J. Johnsen, A. W. Hansen, and N. Balling (1998), Past temperatures directly from the Greenland Ice Sheet, *Science*, *282*(5387), 268–271.

Dahl-Jensen, D., N. Gundestrup, S. P. Gogineni, and H. Miller (2003), Basal melt at NorthGRIP modeled from borehole, ice-core and radio-echo sounder observations, *Ann. Glaciol.*, *37*, 207–212.

Davis, J. L., and A. P. Annan (1989), Ground-penetrating radar for high-resolution mapping of soil and rock stratigraphy, *Geophys. Prosp.*, *37*, 531–551.

Drews, R., O. Eisen, I., S. Kipfstuhl, A. Lambrecht, D. Steinhage, F. Wilhelms, and H. Miller (2009), Layer disturbances and the radio-echo free zone in ice sheets, *The Cyrosphere*, *3*, 195–203, doi:10.5194/tcd-3-307-2009.

Eisen, O., F. Wilhelms, U. Nixdorf, and H. Miller (2003), Revealing the nature of radar reflections in ice: DEP-based FDTD forward modeling, *Geophys. Res. Lett.*, *30*(5), 1218, doi:10.1029/2002GL016403.

Ettema, J., M. R. van den Broeke, E. van Meijgaard, W. J. van de Berg, J. L. Bamber, J. E. Box, and R. C. Bales (2009), Higher surface mass balance of the Greenland Ice Sheet revealed by high-resolution climate modeling, *Geophys. Res. Lett.*, *36*, L12501, doi:10.1029/2009GL038110.

Engelhardt, H. (2004), Thermal regime and dynamics of the West Antarctic ice sheet, *Ann. Glaciol.*, *39*, 85–92.

Fahnestock, M., W. Abdalati, I. Joughin, J. Brozena, and P. Gogineni (2001), High geothermal heat flow, basal melt, and the origin of the rapid ice flow in central Greenland, *Science*, *294*(5550), 2338–2342.

Fujita, S., H. Maeno, S. Uratsuka, T. Furukawa, S. Mae, Y. Fujii, and O. Watanabe (1999), Nature of radio-echo layering in the Antarctic ice sheet detected by a two-frequency experiment, *J. Geophys. Res.*, *104*(B6), 13,013–13,024, doi:10.1029/1999JB900034.

Fujita, S., T. Matsuoka, T. Ishida, K. Matsuoka, and S. Mae (2000), A summary of the complex dielectric permittivity of ice in the megahertz range and its applications for radar sounding of polar ice sheets, in *Physics of Ice Core Records*, edited by T. Hondoh, pp. 185–212, Hokkaido Univ. Press, Japan.

Fujita, S., et al. (2012), Radar diagnosis of the subglacial conditions in Dronning Maud Land, East Antarctica, *The Cryosphere*, *6*, 1203–1219, doi:10.5194/tc-6-1203-2012.

Funk, M., K. Echelmeyer, and A. Iken (1994), Mechanisms of fast flow in Jakobshavns Isbræ, West Greenland: Part II. Modeling of englacial temperatures, *J. Glaciol.*, *40*(136), 569–585.

Gogineni, S., T. Chuah, C. Allen, K. Jezek, and R. K. Moore (1998), An improved coherent radar depth sounder, *J. Glaciol.*, *44*(148), 659–669.

Greve, R. (2005), Relation of measured basal temperatures and the spatial distribution of the geothermal heat flux for the Greenland ice sheet, *Ann. Glaciol.*, *42*, 424–432.

Gundestrup, N., and B. L. Hansen (1984), Bore-hole survey at DYE 3, South Greenland, *J. Glaciol.*, *30*(106), 282–288.

Hanson, J. C., et al. (2015), Radar absorption, basal reflection, thickness and polarization measurements from the Ross Ice Shelf, Antarctica, *J. Glaciol.*, *61*(227), 438–446, doi:10.3189/2015JoG14J214.

Harrington, J. A., N. F. Humphrey, and J. T. Harper (2015), Temperature distribution and thermal anomalies along a flowline of the Greenland Ice Sheet, *Ann. Glaciol.*, *56*(70), 98–104, doi:10.3189/2015AoG70A945.

Hempel, L., F. Thyssen, N. Gundestrup, H. B. Clausen, and H. Miller (2000), A comparison of radio-echo sounding data and the electrical conductivity of the GRIP ice core, *J. Glaciol.*, *46*(154), 369–374.

Holschuh, N., K. Christianson, and S. Anandakrishnan (2014), Power loss in dipping internal reflectors, imaged using ice-penetrating radar, *Ann. Glaciol.*, *55*(67), 49–56, doi:10.3189/2014AoG67A005.

Hughes, M. (2008), Determination of glacial-ice temperature profiles using radar and an antenna-gain estimation technique, MSc thesis, Univ. Kansas.

Huybrechts, P. (1994), The present evolution of the Greenland ice sheet: An assessment by modelling, *Global Planet. Change*, *9*, 39–51.

Jacobel, R. W., and B. C. Welch (2005), A time marker at 17.5 kyr detected throughout West Antarctica, *Ann. Glaciol.*, *41*, 47–51.

Jacobel, R. W., B. C. Welch, D. Osterhouse, R. Pettersson, and J. A. MacGregor (2009), Spatial variation of radar-derived basal conditions on Kamb Ice Stream, West Antarctica, *Ann. Glaciol.*, *50*(51), 10–16.

Jacobel, R. W., K. E. Lapo, J. R. Stamp, B. W. Youngblood, B. C. Welch, and J. L. Bamber (2010), A comparison of bed reflectivity and velocity in East Antarctica, *The Cryosphere*, *4*, 447–452, doi:10.5194/tc-4-447-2010.

Johari, G. P., and P. A. Charette (1975), The permittivity and attenuation in polycrystalline and single-crystal ice Ih at 35 and 60 MHz, *J. Glaciol.*, *14*(71), 293–303.

Karlsson, N. B., D. Dahl-Jensen, S. P. Gogineni, and J. D. Paden (2013), Tracing the depth of the Holocene ice in North Greenland from radio-echo sounding data, *Ann. Glaciol.*, *54*(64), 44–50, doi:10.3189/2013AoG64A057.

Kawada, S. (1978), Dielectric anisotropy in ice Ih, *J. Phys. Soc. Jpn.*, *44*(6), 1881–1886.

Larour, E., J. Utke, B. Csatho, A. Schenk, H. Seroussi, M. Morlighem, E. Rignot, N. Schlegel, and A. Khazendar (2014), Inferred basal friction and surface mass balance of the Northeast Greenland Ice Stream using data assimilation of ICESat (Ice Cloud and land Elevation Satellite) surface altimetry and ISSM (Ice Sheet System Model), *The Cyrosphere*, *8*, 2335–2351, doi:10.5194/tc-8-2335-2014.

Legrand, M. R., and M. de Angelis (1996), Light carboxylic acids in Greenland ice: A record of past forest fires and vegetation emissions from the boreal zone, *J. Geophys. Res.*, *101*, 4129–4145, doi:10.1029/95JD03296.

Legrand, M., and P. Mayewski (1997), Glaciochemistry of polar ice cores: A review, *Rev. Geophys.*, *35*(3), 219–243, doi:10.1029/96RG03527.

Lewis, C., S. Gogineni, F. Rodriguez-Morales, B. Panzer, T. Stumpf, J. Paden, and C. Leuschen (2015), Airborne fine-resolution UHF radar: an approach to the study of englacial reflections, firn compaction and ice attenuation rates, *J. Glaciol.*, *61*(225), 89–100, doi:10.3189/2015JoG14J098.

Lüthi, M. P., M. Funk, A. Iken, S. Gogineni, and M. Truffer (2002), Mechanisms of fast flow in Jakobshavn Isbræ, West Greenland: Part III. Measurements of ice deformation, temperature and cross-borehole conductivity in boreholes to the bedrock, *J. Glaciol.*, *48*(162), 369–385.

Lüthi, M. P., et al. (2015), Heat sources within the Greenland Ice Sheet: Dissipation, temperate paleo-firn and cyro-hydrologic warming, *The Cyrosphere.*, *9*, 245–253, doi:10.5194/tc-9-245-2015.

MacGregor, J. A., D. P. Winebrenner, H. Conway, K. Matsuoka, P. A. Mayewski, and G. D. Clow (2007), Modeling englacial radar attenuation at Siple Dome, West Antarctica, using ice chemistry and temperature data, *J. Geophys. Res.*, *112*, F03008, doi:10.1029/2006JF000717.

MacGregor, J. A., S. Anandakrishnan, G. A. Catania, and D. P. Winebrenner (2011), The grounding zone of the Ross Ice Shelf, West Antarctica, from ice-penetrating radar, *J. Glaciol.*, *57*(205), 917–928.

MacGregor, J. A., K. Matsuoka, E. D. Waddington, D. P. Winebrenner, and F. Pattyn (2012), Spatial variation of englacial radar attenuation: Modeling approach and application to the Vostok flowline, *J. Geophys. Res.*, *117*, F03022, doi:10.1029/2011JF002327.

MacGregor, J. A., et al. (2015), Radiostratigraphy and age structure of the Greenland Ice Sheet, *J. Geophys. Res. Earth Surf.*, *120*, doi:10.1002/2014JF003215.

Matsuoka, K. (2011), Pitfalls in radar diagnosis of ice-sheet bed conditions: Lessons from englacial attenuation models, *Geophys. Res. Lett.*, *38*, L05505, doi:10.1029/2010GL046205.

Matsuoka, K., S. Fujita, T. Matsuoka, T. Ishida, T. Hondoh, and S. Mae (1996), Measurements of the complex permittivity of acid-doped ice from 1 kHz to 30 MHz—New data set for developing ice-radar and dielectric analysis of ice cores, *Proc. Natl. Inst. Polar Res. Symp. Polar Meteorol. Glaciol.*, *10*, 25–35.

Matsuoka, K., L. Wilen, S. P. Hurley, and C. F. Raymond (2009), Effects of birefringence within ice sheets on obliquely propagating radio waves, *IEEE Trans. Geosci. Remote. Sens.*, *47*(5), 1429–1443, doi:10.1109/TGRS.2008.2005201.

Matsuoka, K., T. Furukawa, S. Fujita, H. Maeno, S. Uratsuka, R. Naruse, and S. Mae (2003), Crystal orientation fabrics within the Antarctic ice sheet revealed by a multipolarization plane and dual-frequency radar survey, *J. Geophys. Res.*, *108*(B10), 2499, doi:10.1029/2003JB002425.

Matsuoka, K., J. A. MacGregor, and F. Pattyn (2010a), Using englacial radar attenuation to better diagnose the subglacial environment: A review, *Proc. 13th Int. Conf. GPR*, 482–486, doi:10.1109/ICGPR.2010.5550161.

Matsuoka, K., D. Morse, and C. F. Raymond (2010b), Estimating englacial radar attenuation using depth profiles of the returned power, central West Antarctica, *J. Geophys. Res.*, *115*, F02012, doi:10.1029/2009JF001496.

Matsuoka, K., J. A. MacGregor, and F. Pattyn (2012), Predicting radar attenuation across Antarctica, *Earth Planet. Sci. Lett.*, *359–360*, 173–183, doi:10.1016/j.epsl.2012.10.018.

Medley, B., et al. (2013), Airborne-radar and ice-core observations of annual snow accumulation over Thwaites Glacier, West Antarctica confirm the spatiotemporal variability of global and regional atmospheric models, *Geophys. Res. Lett.*, *40*, 3649–3654, doi:10.1002/grl.50706.

Meese, D. A., A. J. Gow, P. Grootes, M. Stuiver, P. A. Mayewski, G. A. Zielinski, M. Ram, K. C. Taylor, and E. D. Waddington (1994), The accumulation record from the GISP2 core as an indicator of climate change throughout the Holocene, *Science*, *266*, 1680–1682.

Moore, J. C., and S. Fujita (1993), Dielectric properties of ice containing acid and salt impurity at microwave and low frequencies, *J. Geophys. Res.*, *98*(B6), 9769–9780, doi:10.1029/93JB00710.

Moore, J. C., E. W. Wolff, H. B. Clausen, C. U. Hammer, M. R. Legrand, and K. Fuhrer (1994), Electrical response of the Summit-Greenland ice core to ammonium, sulphuric acid, and hydrochloric acid, *Geophys. Res. Lett.*, *21*(7), 565–568, doi:10.1029/94GL00542.

NEEM community members (2013), Eemian interglacial reconstructed from a Greenland folded ice core, *Nature*, *493*(7433), 489–494, doi:10.1038/nature11789.

Nowicki, S., et al. (2013), Insights into spatial sensitivities of ice mass response to environmental change from the SeaRISE ice sheet modeling project II: Greenland, *J. Geophys. Res. Earth Surf.*, *118*, 1025–1044, doi:10.1002/jgrf.20076.

Oswald, G. K. A., and S. P. Gogineni (2012), Mapping basal melt under the northern Greenland Ice Sheet, *IEEE Trans. Geosci. Remote Sens.*, *50*(2), 585–592, doi:10.1109/TGRS.20110.2162072.

Paden, J. D., C. T. Allen, S. Gogineni, K. C. Jezek, D. Dahl-Jensen, and L. B. Larsen (2005), Wideband measurements of ice sheet attenuation and basal scattering, *IEEE Geosci. Remote Sens. Lett.*, *2*(2), 164–168, doi:10.1109/LGRS.2004.842474.

Paren, J. G. (1981), Reflection coefficient at a dielectric interface, *J. Glaciol.*, *27*(95), 203–204.

Pattyn, F. (2010), Antarctic subglacial conditions inferred from a hybrid ice sheet/ice stream model, *Earth Planet. Sci. Lett.*, *295*, 451–460, doi:10.1016/j.epsl.2010.04.025.

Peters, L. E., S. Anandakrishnan, R. B. Alley, and D. E. Voigt (2012), Seismic attenuation in glacial ice: A proxy for englacial temperature, *J. Geophys. Res.*, *117*, F02008, doi:10.1029/2011JF002201.

Petrunin, A. G., I. Rogozhina, A. P. M. Vaughan, I. T. Kukkonen, M. K. Kaban, I. Koulakov, and M. Thomas (2013), Heat flux variations beneath central Greenland's ice due to anomalously thin lithosphere, *Nat. Geosci.*, *6*(9), 746–750, doi:10.1038/ngeo.1898.

Rasmussen, S. O., et al. (2013), A first chronology for the North Greenland Eemian Ice Drilling (NEEM) ice core, *Clim. Past*, *9*, 2713–2730, doi:10.5194/cp-9-2713-2013.

Robin, G. d. Q., S. Evans, and J. T. Bailey (1969), Interpretation of radio echo sounding in polar ice sheets, *Philos. Trans. R. Soc. London, Ser. A*, *265*(1166), 437–505.

Rodríguez-Morales, F., et al. (2014), Advanced multifrequency radar instrumentation for polar research, *IEEE Trans. Geosci. Remote Sens.*, *52*(5), 2824–2842, doi:10.1109/TGRS.2013.2266415.

Rogozhina, I., Z. Martinec, J. M. Hagedoorn, M. Thomas, and K. Fleming (2011), On the long-term memory of the Greenland Ice Sheet, *J. Geophys. Res.*, *116*, F01011, doi:10.1029/2010JF001787.

Rogozhina, I., J. M. Hagedoorn, Z. Martinec, K. Fleming, O. Soucek, R. Greve, and M. Thomas (2012), Effects of uncertainties in the geothermal heat flux distribution on the Greenland Ice Sheet: An assessment of existing heat flow models, *J. Geophys. Res.*, *117*, F02025, doi:10.1029/2011JF002098.

Schroeder, D. M., D. D. Blankenship, and D. A. Young (2013), Evidence for a water system transition beneath Thwaites Glacier, West Antarctica, *Proc. Natl. Acad. Sci. U. S. A.*, *110*(30), 12,225–12,228, doi:10.1073/pnas.1302828110.

Schroeder, D. M., D. D. Blankenship, D. A. Young, and E. Quartini (2014), Evidence for elevated and spatially variable geothermal flux beneath the West Antarctic Ice Sheet, *Proc. Natl. Acad. Sci. U.S.A.*, *111*(25), 9070–9072, doi:10.1073/pnas.1405184111.

Seroussi, H., M. Morlighem, E. Rignot, A. Khazendar, E. Larour, and J. Mouginot (2013), Dependence of century-scale projections of the Greenland ice sheet on its thermal regime, *J. Glaciol.*, *59*(218), 1024–1034, doi:10.3189/2013JoG13J054.

Stillman, D. E., J. A. MacGregor, and R. E. Grimm (2013a), The role of acids in electrical conduction through ice, *J. Geophys. Res. Earth Surf.*, *118*, 1–16, doi:10.1029/2012JF002603.

Stillman, D. E., J. A. MacGregor, and R. E. Grimm (2013b), Electrical response of ammonium-rich water ice, *Ann. Glaciol.*, *54*(64), 21–26, doi:10.3189/2013AoG64A204.

Winebrenner, D. P., B. E. Smith, G. A. Catania, H. B. Conway, and C. F. Raymond (2003), Radio-frequency attenuation beneath Siple Dome, West Antarctica, from wide-angle and profiling radar observations, *Ann. Glaciol.*, *37*, 226–232.

Weertman, J. (1968), Comparison between measured and theoretical temperature profiles of the Camp Century, Greenland, borehole, *J. Geophys. Res.*, *73*(8), 2691–2700, doi:10.1029/JB073i008p02691.

Wolff, E. W., W. D. Miners, J. C. Moore, and J. G. Paren (1997), Factors controlling the electrical conductivity of ice from the polar regions—A summary, *J. Phys. Chem. B*, *101*(32), 6090–6094.

Zirizzotti, A., L. Cafarella, S. Urbini, and J. A. Baskaradas (2014), Electromagnetic ice absorption rate at Dome C, Antarctica, *J. Glaciol.*, *60*(223), 849–854, doi:10.3189/2014JoG12J208.